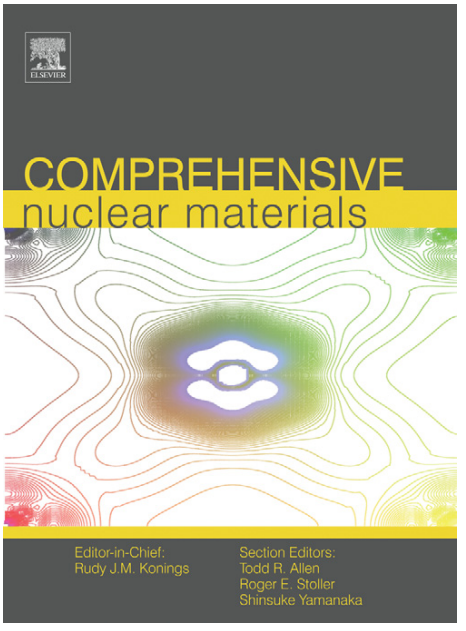

Zinkle S.J. (2012) Radiation-Induced Effects on Microstructure. In: Konings R.J.M., (ed.) Comprehensive Nuclear Materials, volume 1, pp. 65-98 Amsterdam: Elsevier.

1.03 Radiation-Induced Effects on Microstructure*

S. J. Zinkle
Oak Ridge National Laboratory, Oak Ridge, TN, USA

Abbreviations

appm	Atomic parts per million
bcc	Body-centered cubic
dpa	Displacements per atom
fcc	Face-centered cubic
HCP	Hexagonal close packed
MD	Molecular dynamics
PKA	Primary knock-on atom
RIS	Radiation induced segregation
SIA	Self-interstitial atom
SFT	Stacking fault tetrahedron

*Prepared for the Oak Ridge National Laboratory under Contract No. DE-AC05-000R22725

TEM	Transmission electron microscope
T_M	Melting temperature

1.03.1 Introduction

Irradiation of materials with particles that are sufficiently energetic to create atomic displacements can induce significant microstructural alteration, ranging from crystalline-to-amorphous phase transitions to the generation of large concentrations of point defect or solute aggregates in crystalline lattices. These microstructural changes typically cause significant changes in the physical and mechanical properties of the irradiated material. A variety of advanced microstructural characterization tools are available to examine the microstructural changes induced by particle irradiation, including electron microscopy, atom probe field ion microscopy, X-ray scattering and spectrometry, Rutherford backscattering spectrometry, nuclear reaction analysis, and neutron scattering and spectrometry.[1,2] Numerous reviews, which summarize the microstructural changes in materials associated with electron[3–6] and heavy ion or neutron[4,7–20] irradiation, have been published. These reviews have focused on pure metals[5–10,12–14,16,19] as well as model alloys,[3,9,13,14] steels,[11,20] and ceramic[3,4,15,17,18] materials.

In this chapter, the commonly observed defect cluster morphologies produced by particle irradiation are summarized and an overview is presented on some of the key physical parameters that have a major influence on microstructural evolution of irradiated materials. The relationship between microstructural changes and evolution of physical and mechanical properties is then summarized, with particular emphasis on eight key radiation-induced property degradation phenomena. Typical examples of irradiated microstructures of metals and ceramic materials are presented. Radiation-induced changes in the microstructure of organic materials such as polymers are not discussed in this overview.

1.03.2 Overview of Defect Cluster Geometries in Irradiated Materials

A wide range of defect cluster morphologies can be created by particle irradiation.[8,21,22] The thermodynamic stability of these defect cluster geometries is dependent on the host material and defect cluster size as well as the potential presence of impurities. There are four common geometric configurations for clusters of vacancies and self-interstitial atoms (SIAs): two planar dislocation loop configurations (faulted and perfect loops) that occur for both vacancies and SIAs, and two three-dimensional configurations that occur only for vacancy clusters (the stacking fault tetrahedron, SFT, and cavities).

The faulted loop (also called Frank loop) is most easily visualized as either insertion or removal of a layer of atoms, creating a corresponding extrinsic or intrinsic stacking fault associated with condensation of a planar monolayer of vacancies and SIAs, respectively. The faulted loop generally forms on close packed planes, i.e., {111} habit planes with a Burgers vector of $b = 1/3\langle 111\rangle$ for face-centered cubic (fcc) materials, {110} habit planes with $b = 1/2\langle 110\rangle$ for body-centered cubic (bcc) metals, and $\{10\bar{1}0\}$ habit planes with $b = a/2\ \langle 10\bar{1}0\rangle$ for hexagonal close packed (HCP) metals.[23] Faulted loops with $b = a/2$ [0001] on the (0001) basal plane are also observed in many irradiated HCP materials. All of these faulted loops are immobile (sessile). The high stacking fault energy of bcc metals inhibits faulted loop nucleation and growth, and favors formation of perfect loops. There have been several observations of faulted loops consisting of multiple atomic layers.[8,21]

The perfect loop in fcc materials is typically created from initially formed faulted loops by nucleation of an $a/6\langle 112\rangle$ Shockley partial dislocation that sweeps across the surface of the faulted loop and thereby restores perfect stacking order by this atomic shear of one layer of atoms. The resultant Burgers vector in fcc materials is $a/2\langle 110\rangle$, maintaining the {111} loop habit planes. After unfaulting, rotation on the glide cylinder gradually changes the habit plane of the fcc perfect loop from {111} to {110} to create a pure edge loop geometry. After the loop rotates to the {110} habit plane, the perfect loop is glissile. Experimental studies of irradiated fcc materials typically observe perfect loops on either {111} or {110} habit planes (or both), depending on the stage of the glide cylinder rotation process. The glissile perfect loop configurations for bcc materials consist of $b = a/2\langle 111\rangle$ loops on {111} habit planes and $b = a\langle 100\rangle$ loops on {100} habit planes. The typical corresponding HCP perfect loop configuration is $b = a/3\ \langle 11\bar{2}0\rangle$ on $\{11\bar{2}0\}$ prismatic habit planes.

SFTs are only observed in close-packed cubic structures (i.e. fcc materials). The classic Silcox–Hirsch[24] mechanism for SFT formation is based on dissociation of $b = 1/3\langle 111\rangle$ faulted loops into $a/6\langle 110\rangle$ stair rod and $a/6\langle 121\rangle$ Shockley partial dislocations on the acute intersecting {111} planes. Interaction between the climbing Shockley partials creates $a/6\langle 011\rangle$ stair rod dislocations along the

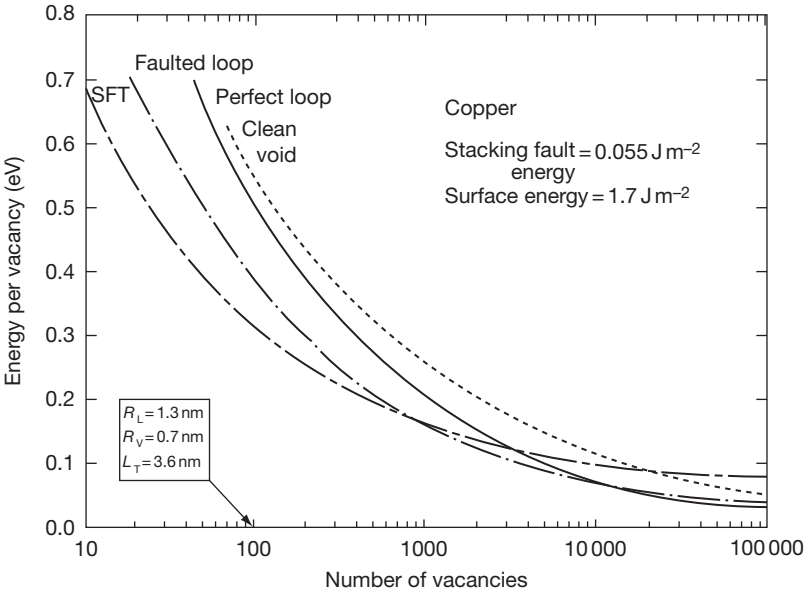

Figure 1 Comparison of calculated size-dependent energies for different vacancy cluster geometries in pure copper. Reproduced from Zinkle, S. J.; Seitzman, L. E.; Wolfer, W. G., *Philos. Mag. A* **1987**, 55(1), 111–125.

tetrahedron edges. The Silcox–Hirsch mechanism has been verified during *in situ* transmission electron microscope (TEM) observation of vacancy loops in quenched gold.[25] Evidence from molecular dynamics (MD) simulations[26–29] and TEM observations[12,19,30–32] during *in situ* or postirradiation studies indicate that SFT formation can occur directly within the vacancy-rich cascade core during the 'thermal spike' phase of energetic displacement cascades.

There is an important distinction between the definitions for the terms void, bubble, and cavity, all of which describe a three-dimensional vacancy cluster that is roughly spherical in shape. Void refers to an object whose stability is not dependent on the presence of internal pressurization from a gaseous species such as helium. Bubbles are defined as pressurized cavities. The term cavity can be used to refer to either voids or bubbles and is often used as a generic term for both cases. In many cases, voids exhibit facets (e.g. truncated octahedron for fcc metals) that correspond with close-packed planes of the host lattice, whereas bubbles are generally spherical in shape. However, the absence of facets cannot be used as conclusive evidence to discriminate between a void and a bubble.

Figure 1 shows the calculated energy for different vacancy geometries in pure fcc copper.[22] The SFT is calculated to be the most energetically favorable configuration in copper for small sizes (up to about 4 nm edge lengths). Faulted loops are calculated to be stable at intermediate sizes, and perfect loops are calculated to be most stable at larger sizes. In practice, many metastable defect cluster geometries may occur. For example, it is well established that the transition from faulted to perfect loops is typically triggered by localized stress such as physical impingement of adjoining loops, and not simply by loop energies; the activation energy barrier for unfaulting may be on the order of 1 eV atom^{-1}.[8] Similarly, large activation energy barriers exist for the conversion between planar loops and voids.[33]

1.03.3 Influence of Experimental Conditions on Irradiated Microstructure

1.03.3.1 Irradiation Dose

As discussed in **Chapter 1.01, Fundamental Properties of Defects in Metals**; **Chapter 1.02, Fundamental Point Defect Properties in Ceramics**; and **Chapter 1.11, Primary Radiation Damage Formation**, the international standardized displacement per atom (dpa) unit for radiation damage[34] is a useful parameter for comparing displacement damage levels in a variety of irradiation environments. The calculated damage level is directly proportional to the product of the fluence and the average kinetic energy transferred to the host lattice atoms (damage energy). The effective damage cross-sections for 1 MeV particles incident on copper range from ~30 barns (1 barn = 1×10^{-24} cm^2) for electrons[35] to ~600 barns for neutrons[36] and $\sim 2 \times 10^9$ barns for Cu ions.[37]

The dpa unit is remarkably effective in correlating the initial damage production levels over a wide range of materials and irradiating particles and is the singular most important parameter for quantifying radiation effects in materials. Numerous aspects of microstructural evolution are qualitatively equivalent on a dpa basis for materials irradiated in widely different irradiation environments. However, the dpa unit does not accurately capture some of the complex differences in primary damage production for energetic displacement cascade conditions compared to isolated Frenkel pair production.[38] For example, defect production at cryogenic temperatures (where long-range defect migration and annihilation does not occur) for neutron and heavy ion-irradiated materials is about 20–30% of the calculated dpa value due to athermal in-cascade recombination processes.[38,39] In addition, the accumulated damage, as evident in the form of point defect clusters or other microstructural features, typically exhibits a complex nonlinear relationship with irradiation dose that depends on irradiation temperature and several other factors. The impact of other experimental variables on the dose-dependent damage accumulation behavior is discussed in Sections 1.03.3.2–1.03.3.9.

1.03.3.2 Role of Primary Knock-on Atom (PKA) Spectra

Displacement damage can occur in materials when the energy transferred to lattice atoms exceeds a critical value known as the threshold displacement energy (E_d), which has a typical value of 30–50 eV.[8,18,40] Figure 2 shows an example of the effect of bombarding energy on the microstructure of CeO_2 during electron irradiation near room temperature.[41] The loop density increases rapidly with increasing energy above 200 keV, suggesting that 200 keV electrons transfer elastic energy that is slightly above the threshold displacement energy. High-resolution microstructural analysis determined that the dislocation loops were associated with aggregation of oxygen ions only (i.e., no Ce displacement damage) for electron energies up to 1250 keV, whereas perfect interstitial-type dislocation loops were formed for electron energies of 1500 keV and higher. Therefore, the corresponding displacement energies in CeO_2 are ~30 and ~50 eV for the O and Ce sublattices, respectively.[41]

A wide range of PKA energies can be achieved during irradiation, depending on the type and energy of irradiating particle. For example, the average PKA energies transferred to a Cu lattice for 1 MeV electrons, protons, Ne ions, Xe ions, and neutrons are 25 eV, 0.5 keV, 9 keV, 50 keV, and 45 keV, respectively.[42] Irradiation of materials with electrons and light ions introduces predominantly isolated SIAs and vacancies (together known as Frenkel pairs) and small clusters of these point defects, because of the low average recoil atom energies of ~0.1–1 keV. Conversely, energetic neutron or heavy ion irradiations produce energetic displacement cascades that can lead to direct formation of defect clusters within isolated displacement cascades due to more energetic average recoil atom energies that exceed 10 keV. Figure 3 compares the weighted PKA energy values for several irradiation species.[40,42]

These differences in PKA energy produce significant changes in primary damage state that can have a pronounced effect on the microstructural evolution observed during irradiation. As briefly mentioned in Section 1.03.3.1, the defect production efficiency per dpa determined from electrical resistivity measurements during irradiation near absolute zero and MD simulation studies is significantly lower (by about

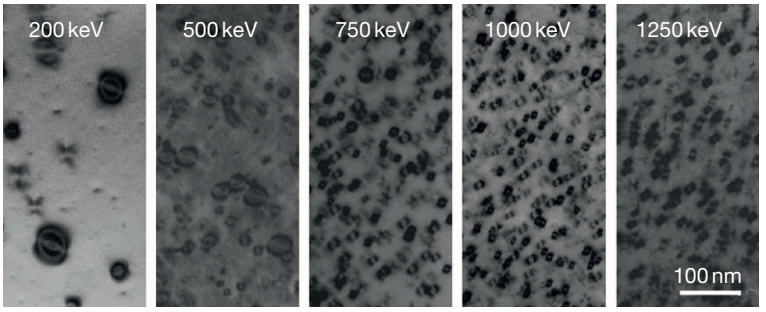

Figure 2 Bright-field images of interstitial-type nonstoichiometric dislocation loops formed in CeO_2 during 200–1250 keV electron irradiation to a fluence of $\sim 3 \times 10^{26}$ electrons per square meter at room temperature. The beam direction is along [011] and the diffraction vector is $g = 11\bar{1}$. Reproduced from Yasunaga, K.; Yasuda, K.; Matsumura, S.; Sonoda, T. *Nucl. Instrum. Methods Phys. Res. B* **2008**, *266*(12–13), 2877–2881.

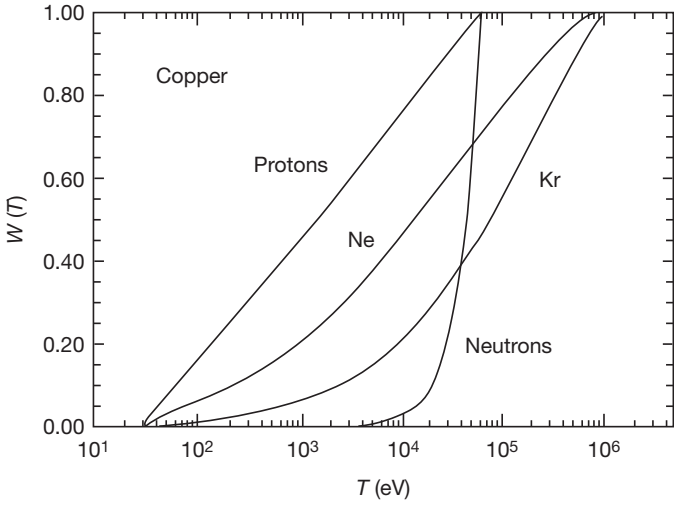

Figure 3 Weighted average recoil atom energy for 1 MeV particles in copper, plotted as a function of recoil energy (T). Reproduced from Averback, R. S. *J. Nucl. Mater.* **1994**, *216*, 49–62.

a factor of 3–4) for energetic displacement cascade conditions compared to isolated Frenkel pair conditions, due to pronounced in-cascade recombination and clustering processes.[38,39] MD computer simulations[43–46] and *in situ* or postirradiation thin foil experimental studies[13,14,47,48] (where interaction between different displacement damage events is minimal due to the strong influence of the surface as a point defect sink) have found that defect clusters visible by transmission electron microscopy (TEM) can be produced directly in displacement cascades if the average PKA energy exceeds 5–10 keV. Irradiations with particles having significantly lower PKA energies typically produce isolated Frenkel pairs and submicroscopic defect clusters that can nucleate and coarsen via diffusional processes. The microstructural evolution of an irradiated material is controlled by different kinetic equations if initial defect clustering occurs directly within the displacement cascade (~0.1–1 ps timescale) versus three-dimensional random walk diffusion to produce defect cluster nucleation and growth, particularly if some of the in-cascade created defect clusters exhibit one-dimensional glide.[49–52] As discussed in **Chapter 1.13, Radiation Damage Theory**, this can produce significant differences in the microstructural evolution for features such as voids and dislocation loops. **Figure 4** compares the microstructure produced in copper following irradiation near 200 °C with fission neutrons[53] and 1 MeV electrons.[54,55] Vacancies and SIAs are fully mobile in copper at this temperature. The 1 MeV electron produces a steady flux of point defects that leads to the

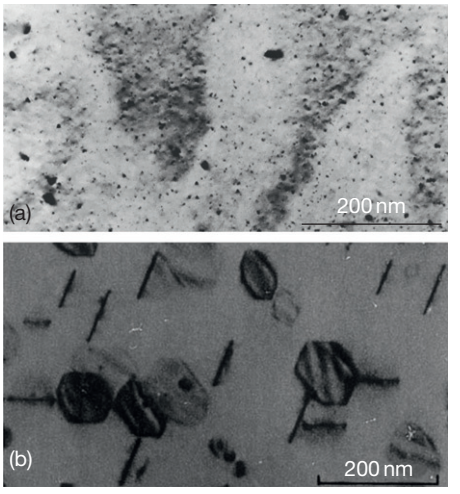

Figure 4 Comparison of the microstructure of copper irradiated near 200 °C with (a) fission neutrons (reproduced from Zinkle, S. J.; Sindelar, R. L. *J. Nucl. Mater.* **1988**, *155–157*, 1196–1200) and (b) 1 MeV electrons (modified from Kiritani, M. *Ultramicroscopy* **1991**, *39*(1–4), 180–186; Kiritani, M.; Takata, H. *J. Nucl. Mater.* **1978,** *69–70*, 277–309).

creation of a moderate density of large faulted interstitial loops. On the other hand, the creation of SFTs and small dislocation loops directly in fission neutron displacement cascades creates a high density ($\sim 2 \times 10^{23}\,m^{-3}$) of small defect clusters, and the high point defect sink strength associated with these defect clusters inhibits the growth of dislocation loops. As shown in **Figure 4**, the net result is a dramatic qualitative and quantitative

difference in the irradiated microstructure due to differences in the PKA spectrum.

Electron microscopy[48,56] and binary collision[48,57] and MD simulation[45] studies have found that irradiation with PKA energies above a critical material-dependent value of ~10–50 keV results in formation of multiple subcascades (rather than an ever-increasing single cascade size), with the size of the largest subcascades being qualitatively similar to an isolated cascade at a PKA energy near the critical value. **Figure 5** compares MD simulations of the peak displacement configurations of PKAs in iron with energies ranging from 1 to 50 keV.[58] At low PKA energies, the size of the displacement cascade increases monotonically with PKA energy. When the PKA energy in Fe exceeds a critical value of ~10 keV, multiple subcascades begin to appear, with the largest subcascade having a size comparable to the 10 keV cascades. The number of subcascades increases with increasing PKA energy, reaching ~5 subcascades for a PKA energy of 50 keV in Fe. A fortunate consequence of subcascade formation is that fission reactor irradiations (~1 MeV neutrons) can be used for initial radiation damage screening studies of potential future fusion reactor (~14 MeV neutrons) materials, since both would have comparable primary damage subcascade structures.[59,60] Further details on the effect of PKA spectrum on primary damage formation are given in **Chapter 1.11, Primary Radiation Damage Formation**.

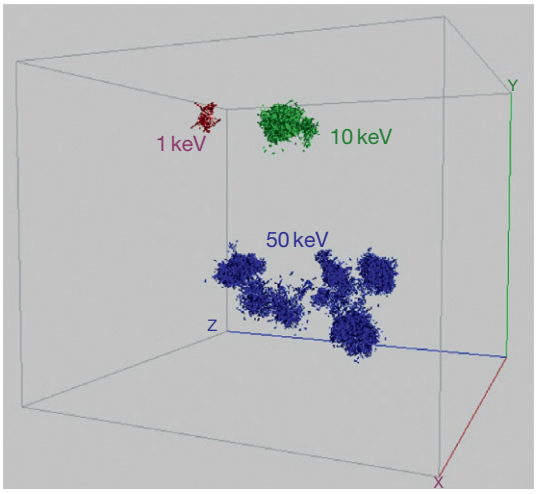

Figure 5 Comparison of the molecular dynamics simulations of 1–50 keV PKA displacement cascades in iron. PKA energies of 1 (red), 10 (green), and 50 (blue) keV for times corresponding to the transient peak number of displaced atoms are shown. The length of the *Z* (horizontal) dimension of the simulation box is 170 lattice parameters (49 nm). Adapted from Stoller, R. E., Oak Ridge National Lab, Private communication, 2010.

1.03.3.3 Role of Irradiation Temperature

Irradiation temperature typically invokes a very large influence on the microstructural evolution of irradiated materials. There are several major temperature regimes delineated by the onset of migration of point defects. Early experimental studies used isochronal annealing electrical resistivity measurements on metals irradiated near absolute zero temperature to identify five major defect recovery stages.[61–64] **Figure 6** shows the five major defect recovery stages for copper irradiated with electrons at 4 K.[65] The quantitative magnitude of the defect recovery in each of the stages generally depends on material, purity, PKA spectrum, and dose. Based on the currently accepted one-interstitial model, Stage I corresponds to the onset of long-range SIA migration. Stage I often consists of several visible substages that have been associated with close-pair (correlated) recombination of Frenkel defects from the same displacement event and long range uncorrelated recombination of defects from different primary displacement events. Stage II involves migration of small SIA clusters and SIA-impurity complexes. Stage III corresponds to the onset of vacancy motion. Stage IV involves migration of vacancy–impurity clusters, and Stage V corresponds to thermal dissociation of sessile vacancy clusters. It should be noted that the specific recovery stage temperature depends on the annealing time (typically 10 or 15 min in the resistivity studies), and therefore needs to be adjusted to lower values when considering the onset temperatures for defect migration in typical

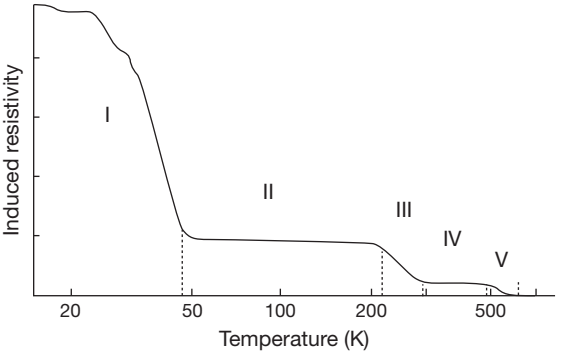

Figure 6 Electrical resistivity defect recovery stages for copper following electron irradiation at 4 K. Reproduced from Agullo-Lopez, F.; Catlow, C. R. A.; Townsend, P. D., *Point Defects in Materials*. Academic Press: San Diego, CA, 1988; p 445.

Table 1 Summary of defect recovery stage temperatures for materials[8,18,63,66–69]

Material	*Melting temperature (K)*	*Crystal structure*	*Stage I (K)*	*Stage III (K)*	*Stage V (K)*
Pb	601	fcc	5	150	300
Al	933	fcc	35	220	
Ag	1233	fcc	35	240	540
Au	1337	fcc	<4	290	530
Cu	1357	fcc	50	270	550
Ni	1726	fcc	60	350	
Pd	1825	fcc	50	~350	
Pt	2045	fcc	30	~350	
Rh	2236	fcc	32	~500	
SiC	3103	cubic	220 (C) 450 (Si)	~1400 (C) 1050 (Si)	
α-Fe	1809	bcc	110	230	
Cr	2130	bcc	40	380	
V	2175	bcc	<6	220	
Nb	2740	bcc	5	230	
Mo	2890	bcc	40	470	
Ta	3287	bcc	10	270	
W	3680	bcc	30	650	
Cd	594	HCP	<4	120	
Zn	693	HCP	18	125	
Mg	922	HCP	13	130	
Ti	1043	HCP	120	250	
Be	1560	HCP	45	280	
Co	1768	HCP	55	310	
Zr	2125	HCP	150	270	
Re	3453	HCP	100	630	1180
Al_2O_3	2324	HCP	~150	~850	

Source: Eyre, B. L. *J. Phys. F* **1973**, 3(2), 422–470.
Zinkle, S. J.; Kinoshita, C. *J. Nucl. Mater.* **1997**, 251, 200–217.
Schilling, W.; Ehrhart, P.; Sonnenberg, K. In *Fundamental Aspects of Radiation Damage in Metals, CONF-751006-P1*; Robinson, M. T.; Young, F. W., Jr., Eds. National Tech. Inform. Service: Springfield, VA, 1975; Vol. I, pp 470–492.
Hautojarvi, P.; Pollanen, L.; Vehanen, A.; Yli-Kauppila, J. *J. Nucl. Mater.* **1983**, *114*(2–3), 250–259.
Lefevre, J.; Costantini, J. M.; Esnouf, S.; Petite, G. *J. Appl. Phys.* **2009**, *106*(8), 083509.
Schultz, H. *Mater. Sci. Eng. A* **1991**, *141*, 149–167.
Xu, Q.; Yoshiie, T.; Mori, H. *J. Nucl. Mater.* **2002**, *307–311*(2), 886–890.
Young, F. W., Jr. *J. Nucl. Mater.* **1978**, *69/70*, 310.
Hoffmann, A.; Willmeroth, A.; Vianden, R. *Z. Phys. B* **1986** *62*, 335.
Takamura, S.; Kobiyama, M. *Rad. Eff. Def. Sol.* **1980**, *49*(4), 247.
Kobiyama, M.; Takamura, S. *Rad. Eff. Def. Sol.* **1985**, *84*(3&4), 161.

neutron irradiation experiments that may occur over time scales of months or years. Table 1 provides a summary of defect recovery stage temperatures for several fcc, bcc, and HCP materials.[8,18,63,66–69] Although there is a general correlation of the recovery temperatures with melting temperature, Table 1 shows there are several significant exceptions. For example, Pt has one of the lowest Stage I temperatures among fcc metals despite having a very high melting temperature. Similarly, Cr has a much higher Stage III temperature than V or Nb that have higher melting points. As illustrated later in this chapter, the microstructures of different materials with the same crystal structure and irradiated within the same recovery stage temperature regime are generally qualitatively similar.

Several analytic kinetic rate theory models have been developed to express the dose dependence of defect cluster accumulation in materials at different temperature regimes.[6,70–72] In the following, summaries are provided on the experimental microstructural observations for five key irradiation temperature regimes.

1.03.3.3.1 Very low temperature regime: immobile SIAs (T<Stage I)

At very low temperatures where defect migration does not occur, defect accumulation is typically proportional to dose until the defect concentration approaches the level where defects created in displacement events begin to overlap and annihilate preexisting defects created earlier in the irradiation

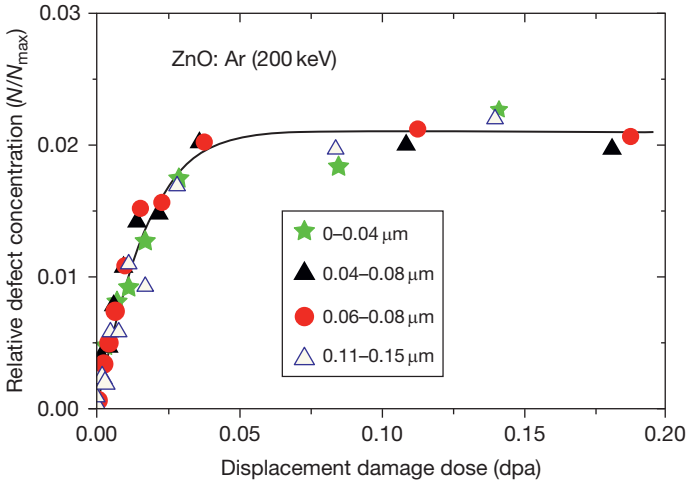

Figure 7 Defect concentration normalized to the total atom concentration N_{max} at four different depths in ZnO irradiated with 200 keV Ar ions at 15 K as determined by Rutherford backscattering spectrometry. Reproduced from Wendler, E.; Bilani, O.; Gärtner, K.; *et al. Nucl. Instrum. Methods Phys. Res. B* **2009**, *267*(16), 2708–2711.

exposure. The defect accumulation kinetics[73] can be described by $N = N_{max}[1 - \exp(-A\phi t)]$, where the parameter A is determined by the spontaneous recombination volume for point defects or the cascade overlap annihilation volume for defect clusters and ϕt is the product of the irradiation flux and time. Due to the lack of defect mobility, defect clusters resolvable by TEM are usually not visible in this irradiation temperature regime unless they are created directly in displacement cascades by energetic PKAs.[74] Saturation in the defect concentration typically occurs after ~0.1 dpa as monitored by atomic disorder,[75–77] electrical resistivity,[78–82] and dimensional change.[83–85] Due to the large increase in free energy associated with lattice disordering and defect accumulation, amorphization typically occurs in this temperature regime in many ceramics[15,85,86] and ordered metallic alloys[87,88] for doses above ~0.1–0.5 dpa. Figure 7 shows an example of the dose-dependent defect concentration in ion-irradiated ZnO at 15 K as determined by Rutherford backscattering spectrometry.[89]

1.03.3.3.2 Low temperature regime: mobile SIAs, immobile vacancies (Stage I<T<Stage III)

Between recovery Stage I and Stage III, the SIA point defects and small SIA clusters have sufficient mobility to migrate and form visible dislocation loops as well as recombine with sessile monovacancies and vacancy clusters. The defect accumulation in this temperature regime is initially linear with dose when the defect concentration is too low for uncorrelated recombination to be a significant contribution, but then transitions to a square root dependence at an intermediate dose in pure materials when interaction between defects from different PKA events becomes important.[6,70–72,90] The critical dose for this kinetic transition is dependent on the concentration of other defect sinks in the lattice (dislocations, grain boundaries, precipitates, etc.). The high sink strength associated with the immobile vacancies limits the growth rate (i.e., size) of the SIA loops for doses above ~0.1 dpa, and the observable defect cluster size and density typically approach a constant value at higher doses. Figure 8 shows an example of the microstructure of AlN following ion irradiation at 80 K (mobile SIAs, immobile vacancies) to a damage level of about 5 dpa.[91] The microstructure consists of small (<5 nm diameter) interstitial dislocation loops.

1.03.3.3.3 Medium temperature regime: mobile SIAs and vacancies (Stage III<T<Stage V)

At temperatures where both SIAs and vacancies are mobile, the defect cluster evolution is complex due to the wide range of defect cluster geometries that can be nucleated.[8,47,92,93] The predominant visible features in this temperature regime are vacancy and interstitial loops and SFTs for irradiated fcc materials and vacancy and interstitial loops and voids for irradiated bcc materials. For medium- to high-atomic number fcc metals exposed to energetic displacement cascades (e.g., fast neutron and heavy ion irradiation), most of the vacancies are tied up in

Figure 8 Weak beam microstructure of dislocation loops in AlN after 2 MeV Si ion irradiation to ~5 dpa at 80 K. The TEM figure is based on irradiated specimens described in Zinkle *et al.*[91]

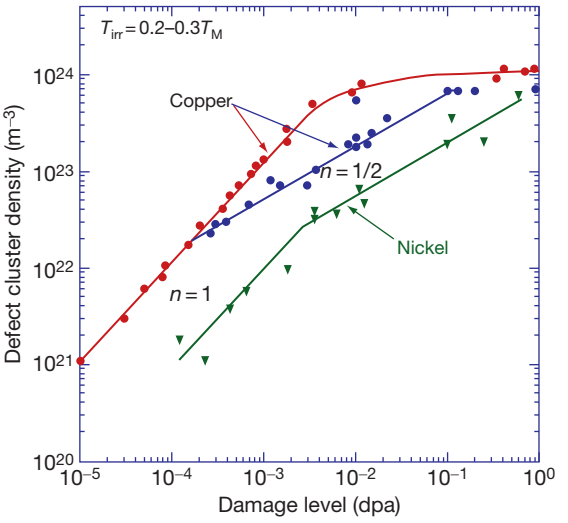

Figure 9 Defect cluster density in neutron-irradiated copper and nickel following fission reactor, 14 MeV, and spallation neutron irradiation near room temperature, as measured by TEM. Depending on the purity of the nominally high-purity copper, the defect cluster accumulation at intermediate doses (~0.001–0.01 dpa) either exhibits a continuation of linear kinetics or switches to a square root accumulation behavior. Based on data reported by Zinkle[94] and Hashimoto *et al.*[95,96]

sessile vacancy clusters (SFTs, vacancy loops) that are formed directly in the displacement cascades. As a consequence, the majority of observed dislocation loops in fcc metals in this temperature and PKA regime are extrinsic (interstitial type), and void nucleation and growth is strongly suppressed. For bcc metals, the amount of in-cascade clustering into sessile defect clusters is less pronounced, and therefore, vacancy loop and void swelling are observed in addition to interstitial dislocation loop evolution. Due to the typical high sink strength of interstitial clusters in this temperature regime, the magnitude of void swelling is generally very small (<1% for doses up to 10 dpa or higher). The loop density and nature in bcc metals is strongly dependent on impurity content in this temperature regime.[5,8,55] For example, the loop concentration in molybdenum irradiated with fission neutrons at 200 °C is much higher in low-purity Mo with ~99% of the loops identified as interstitial type, whereas ~90% of the loops were identified to be vacancy type in high-purity Mo irradiated under the same conditions.[8]

The dose dependence of defect cluster accumulation in this temperature regime is dependent on the material and defect cluster type. For dislocation loops and SFTs in fcc metals, the defect accumulation is initially linear and may exhibit an extended intermediate regime with square root kinetics before reaching a maximum concentration level. The maximum defect cluster density is largely determined by displacement cascade annihilation of preexisting defect clusters. In fcc metals, the defect cluster density may approach $10^{24}\,m^{-3}$, which corresponds to a defect cluster spacing of less than 10 nm and is approximately equal to the maximum diameter of subcascades during the collisional phase in neutron-irradiated metals. As with irradiation near recovery Stage II, the critical dose for transition in defect cluster accumulation kinetics is dependent on the overall defect sink strength. With continued irradiation, the loops may unfault and evolve into network dislocations, particularly if external stress is applied. **Figure 9** summarizes the dose-dependent defect cluster densities in neutron-irradiated copper and nickel.[94–96] In both of these materials, the predominant visible defect cluster was the SFT over the entire investigated dose and temperature regime. Depending on the purity of the copper investigated, the transition from linear to square root accumulation behavior may or may not be evident (cf. the differing behavior for Cu in **Figure 9**). The visible defect cluster density in irradiated copper reaches a constant saturation value (attributed to displacement cascade overlap with preexisting clusters) for damage levels above ~0.1 dpa. The lower visible defect cluster density in Ni compared to Cu at doses up to 1 dpa has been attributed to a longer thermal spike lifetime of the Cu displacement cascades due to inefficient

coupling between electrons and phonons (thereby promoting more complete vacancy and interstitial clustering within the displacement cascade).[97,98]

Figure 10 compares the defect cluster accumulation behavior for two fcc metals (Cu, Ni) and two bcc metals (Fe, Mo) following fission neutron irradiation near room temperature.[30,95,96,99–101] For all four materials, the increase in visible defect cluster density is initially proportional to dose. The visible defect cluster density is highest in Cu over the investigated damage range of 10^{-4}–1 dpa. The irradiated Fe has the lowest visible density at low doses, whereas Ni and Mo have comparable visible cluster densities. At doses above ~0.01 dpa, the visible loop density in Mo decreases due to loop coalescence in connection with the formation of aligned 'rafts' of loops. Partial formation of aligned loop rafts has also been observed in neutron-irradiated Fe for doses near 0.8 dpa, as shown in **Figure 11**.[100] The individual loops within the raft aggregations in neutron-irradiated Fe exhibited the same Burgers vector. The maximum visible cluster density in the fcc metals is about one order of magnitude higher than in the bcc metals (due in part to loop coalescence associated with raft formation). Positron annihilation spectroscopy analyses suggest that submicroscopic cavities are present in the two irradiated bcc metals, with cavity densities that are about two orders of magnitude higher than the visible loop densities.[99–102]

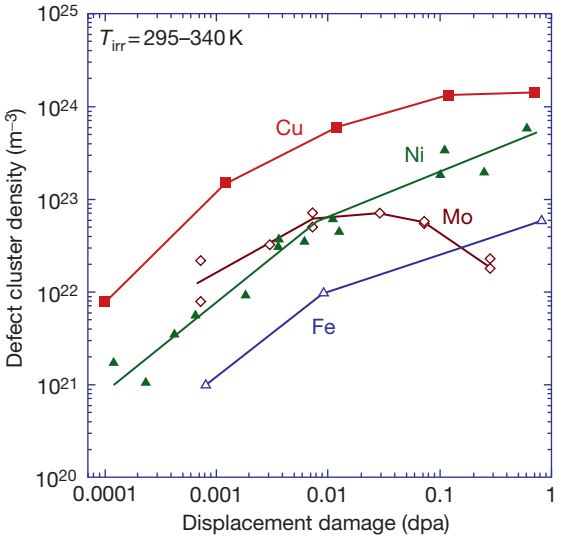

Figure 10 Defect cluster density in copper, nickel, molybdenum, and nickel following fission reactor and 14-MeV neutron irradiation near room temperature, as measured by TEM. Based on data reported by Kiritani[30], Hashimoto *et al.*[95,96], Eldrup *et al.*[99], Zinkle and Singh[100], and Li *et al.*[101]

1.03.3.3.4 High temperature regime: mobile defects and vacancy loop dissociation (T>Stage V)

The typical microstructural features that appear during irradiation at temperatures above recovery Stage V include dislocation loops (vacancy and interstitial type), network dislocations, and cavities. SFTs are thermally unstable in this temperature regime and therefore only SFTs created in the latter stages of the irradiation exposure are visible during postirradiation examination.[94] A variety of precipitates may also be nucleated in irradiated alloys.[11,103–106] Defect cluster accumulation in this temperature regime exhibits

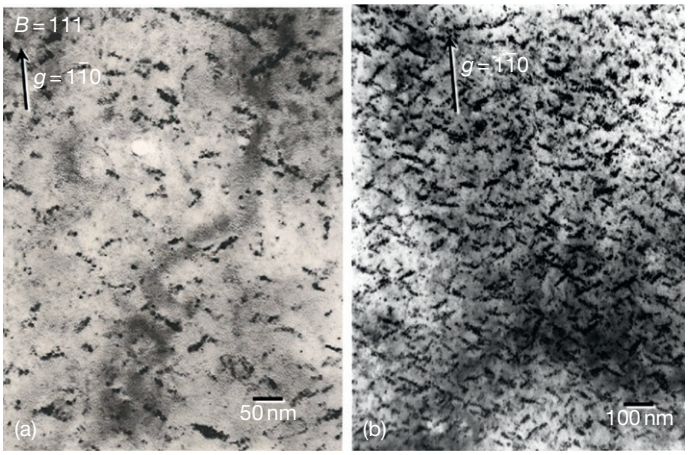

Figure 11 Examples of aligned rafts of dislocation loops in iron following fission neutron irradiation to 0.8 dpa at ~60 °C. The microstructure in thin (a) and thick (b) foil regions are shown. Reproduced from Zinkle, S. J.; Singh, B. N. *J. Nucl. Mater.* **2006**, *351*, 269–284.

several different trends. The visible SIA clusters evolve from a low density of small loops to a saturation density of larger loops after damage levels of ~1–10 dpa. Upon continued irradiation, a moderate density of network dislocations is created due to loop unfaulting and coalescence. The dislocation loop and network dislocation density monotonically decrease with increasing temperature above recovery Stage V,[20,107] whereas the density of precipitates (if present) can either increase or decrease with increasing temperature.

The major microstructural difference from lower temperature irradiations in most materials is the emergence of significant levels of cavity swelling. After an initial transient regime associated with cavity nucleation, a prolonged linear accumulation of vacancies into voids is typically observed.[108,109] The cavity density monotonically decreases with increasing temperature in this temperature regime.[20,107,110] **Figure 12** summarizes the densities of voids and helium bubbles (associated with n,α transmutations) in austenitic stainless steel as a function of fission reactor irradiation temperature for damage rates near 1×10^{-6} dpa s^{-1}.[20] The bubble and void densities exhibit similar temperature dependences in fission reactor-irradiated austenitic stainless steel, with the bubble density approximately one order of magnitude higher than the void density between 400 and 650 °C. For neutron-irradiated copper and Cu–B alloys, the bubble density is similarly observed to be about one order of magnitude larger than the void density for temperatures between 200 and 400 °C.[107,110] At higher temperatures, the void density in copper decreases rapidly and becomes several orders of magnitude smaller than the bubble density. The results from several studies suggest that the lower temperature limits for formation of visible voids[111–113] and helium bubbles[53] can each be reduced by 100 °C or more when the damage rate is decreased to 10^{-9}–10^{-8} dpa s^{-1}, due to enhanced thermal annealing of sessile vacancy clusters during the time to achieve a given dose. Dose rate effects are discussed further in **Section 1.03.3.7**.

The void swelling regime for fcc materials typically extends from 0.35 to $0.6T_M$, where T_M is the melting temperature, with maximum swelling occurring near 0.4–$0.45T_M$ for typical fission reactor neutron damage rates of 10^{-6} dpa s^{-1}.[92,114] **Figure 13** summarizes the temperature-dependent void swelling for neutron-irradiated copper.[110] The results for a neutron-irradiated Cu–B alloy, where ~100 atomic parts per million (appm) He was produced during the 1 dpa irradiation due to thermal neutron transmutation reactions with the B solute, are also shown in this figure.[107] For both materials the onset

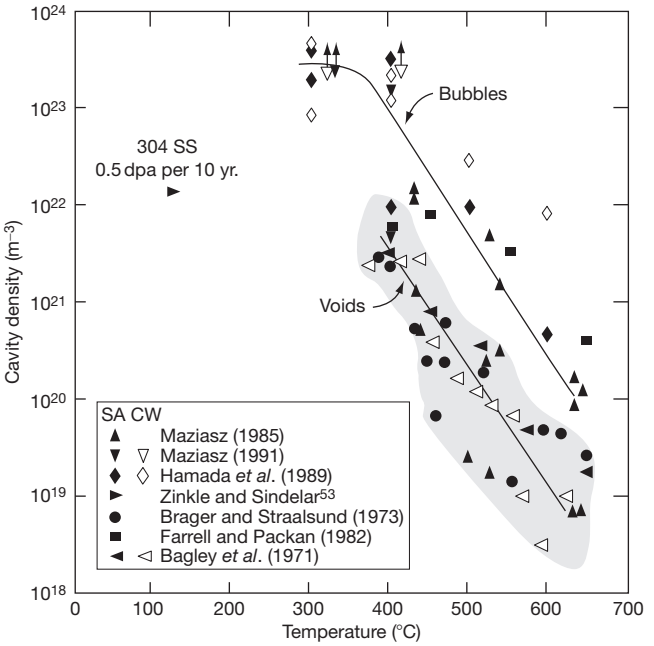

Figure 12 Effect of neutron irradiation temperature on the cavity density observed in austenitic stainless steels for damage rates near 1×10^{-6} dpa s^{-1} (except the labeled data point at 120 °C which had a damage rate of $\sim 10^{-9}$ dpa s^{-1}). Reproduced from Zinkle, S. J.; Maziasz, P. J.; Stoller, R. E. *J. Nucl. Mater.* **1993**, *206*, 266–286.

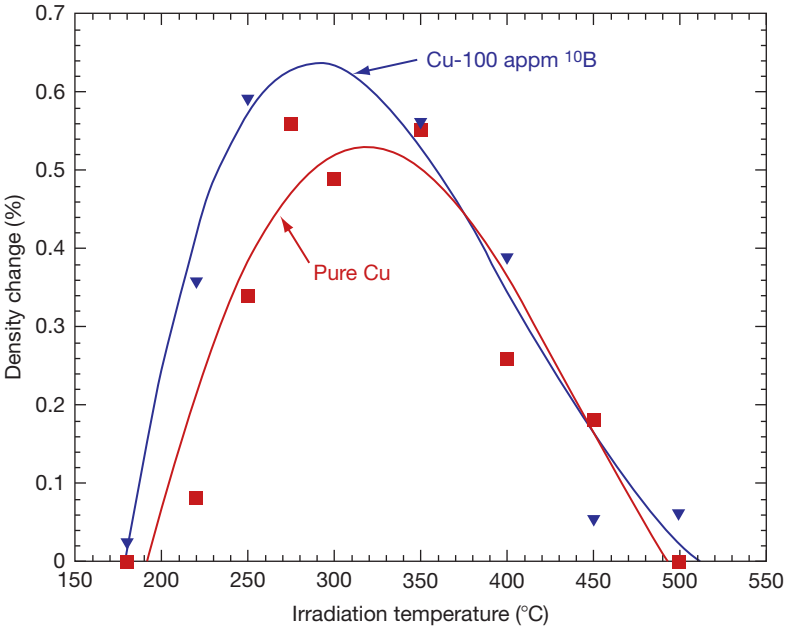

Figure 13 Temperature-dependent void swelling behavior in neutron-irradiated copper and Cu–B alloy after fission neutron irradiation to a dose near 1.1 dpa. Adapted from Zinkle, S. J.; Farrell, K.; Kanazawa, H. *J. Nucl. Mater.* **1991**, *179–181*, 994–997; Zinkle, S. J.; Farrell, K. *J. Nucl. Mater.* **1989**, *168*, 262–267.

of swelling occurs at temperatures near 180 °C, which corresponds to recovery Stage V in Cu for the 2×10^{-7}dpa s^{-1} damage rates in this experiment. The swelling in Cu was negligible for temperatures above ~500 °C, and maximum swelling was observed near 300 °C. The lower temperature limit for swelling in fcc materials is typically controlled by the high point defect sink strength of sessile defect clusters below recovery Stage V. The upper temperature limit is controlled by thermal stability of voids and a reduction in the vacancy supersaturation relative to the equilibrium vacancy concentration.

As noted by Singh and Evans,[92] the temperature dependence of the void swelling behavior of bcc and fcc metals can be significantly different. In particular, due to the lower amount of in-cascade formation of large sessile vacancy clusters in medium-mass bcc metals compared to fcc metals, the recovery Stage V is much less pronounced in bcc metals. The presence of a high concentration of mobile vacancies at temperatures below recovery Stage V (and a concomitant reduction in the density of sessile vacancy-type defect cluster sinks) allows void swelling to occur in bcc metals for temperatures above recovery Stage III (onset of long-range vacancy migration). **Figure 14** compares the temperature dependence of the void swelling behavior of Ni (fcc) and Fe (bcc) after high dose neutron irradiation.[115] Whereas the peak

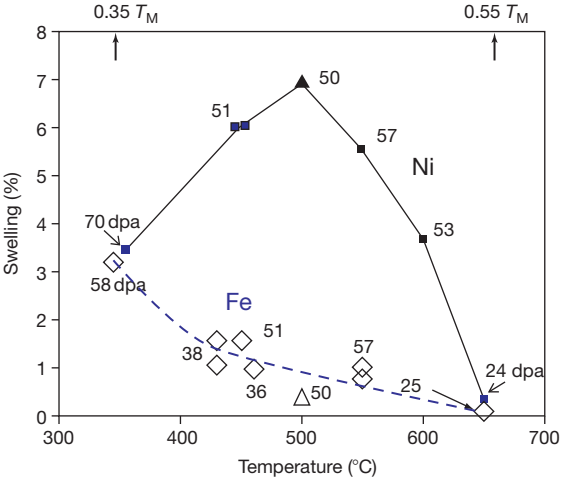

Figure 14 Comparison of the temperature-dependent void swelling behavior in Fe and Ni, based on data reported by Budylkin *et al*.[115]

swelling after ~50 dpa in neutron-irradiated Ni occurred near 0.45 T_M, the peak swelling in Fe occurred at the lowest investigated temperature of ~0.35 T_M. Several other bcc metals including Mo, W, Nb, and Ta exhibit void formation for irradiation temperatures as low as ~0.2 T_M, which is approaching the upper limit of recovery Stage III.[92] It is worth noting the peak swelling temperature for neutron-irradiated bcc metals Mo and Nb–1Zr after exposures of ~50 dpa

occur near 0.3–0.35 T_M,[116,117] which is much lower than the 0.4–0.45 T_M peak swelling temperature observed for fcc metals.

1.03.3.3.5 Very high temperature regime: He cavities (T >> Stage V)

Irradiation at temperatures near or above 0.5 T_M typically results in only minor microstructural changes due to the strong influence of thermodynamic equilibrium processes, unless significant amounts of impurity atoms such as helium are introduced by nuclear transmutation reactions or by accelerator implantation. When helium is present, cavities are nucleated in the grain interior and along grain boundaries. The cavity size increases and the density decreases rapidly with increasing temperature. Figure 15 compares the helium cavity density for various implantation and neutron irradiation conditions in austenitic stainless steels as a function of temperature.[118,119] The temperature dependence of the cavity density is distinguished by two different regimes. At very high temperatures, the cavity density is controlled by gas dissociation mechanisms with a corresponding high activation energy, and at lower temperatures by gas or bubble diffusion kinetics.[118] The cavity density decreases by nearly two orders of magnitude for every 100 K increase in irradiation temperature in this very high temperature regime. The helium cavity densities in materials irradiated at low temperatures (near room temperature) and then annealed at high temperature are typically much higher than in materials irradiated at high temperature, due to excessive cavity nucleation that occurs at low temperature. In the absence of applied stress, the helium-filled cavities tend to nucleate rather homogeneously in the grain interiors and along grain boundaries. If the helium generation and displacement damage occurs in the presence of an applied tensile stress, the helium cavities are preferentially nucleated along grain boundaries and may cause grain boundary embrittlement.[120]

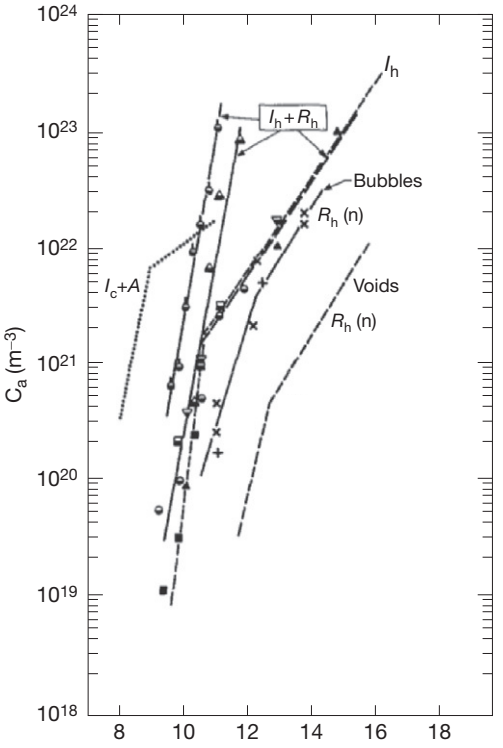

Figure 15 Temperature dependence of observed cavity densities in commercial austenitic steels during He implantation or neutron irradiation at elevated temperatures (I_h and R_h, respectively). The dashed lines denote the densities of voids during neutron irradiation (R_h(n)) and bubbles during implantation near room temperature followed by high temperature annealing (I_c+A). Adapted from Singh, B. N.; Trinkaus, H. *J. Nucl. Mater.* **1992**, *186*, 153–165; Trinkaus, H.; Singh, B. N. *J. Nucl. Mater.* **2003**, *323* (2–3), 229–242.

1.03.3.4 Role of Atomic Weight

Materials with low atomic weight, such as aluminum, exhibit more spatially diffuse displacement cascades than high atomic weight materials due to the increase in nuclear and electronic stopping power with increasing atomic weight. For example, the calculated average vacancy concentration in Au displacement cascades is about two to three times higher than in Al cascades for a wide range of PKA energies.[57] This increased energy density and compactness in the spatial extent of displacement cascades can produce enhanced clustering of point defects within the energetic displacement cascades of high atomic weight materials. Electrical resistivity isochronal annealing studies of fission neutron-irradiated metals have confirmed that the amount of defect recovery during Stage I annealing decreases with increasing atomic weight,[79] which is an indication of enhanced SIA clustering within the displacement cascades. The importance of atomic weight on defect clustering depends on the material-specific critical energy for subcascade formation compared to the average PKA energy. For example, in the fcc noble metal series Cu, Ag, Au, the subcascade formation energy increases slightly with mass (10, 13, and 14 keV, respectively), and very little qualitative difference exists in the defect cluster accumulation behavior of these three materials.[13,56] In general, there is not a universal relation

between atomic weight and microstructural parameters such as overall defect production,[121] defect cluster yield,[122,123] or visible defect cluster size.[56]

1.03.3.5 Role of Crystal Structure

MD simulations[23] predict the absolute level of defect production is not strongly affected by crystal structure. Conversely, electrical resistivity studies of fission neutron-irradiated metals suggest that the overall defect production is highest in HCP metals, intermediate in bcc metals, and lowest in fcc metals,[121] which suggests that the anisotropic nature of HCP crystals might inhibit defect recombination within displacement cascades. TEM measurements of defect cluster yield (number of visible cascades per incident ion) in ion-irradiated metals have found that the relatively few visible defect clusters are formed directly in displacement cascades in bcc metals,[122] whereas cluster formation is relatively efficient in fcc metals and variable behavior is observed for HCP metals.[123] Faulted dislocation loops are often observed in irradiated fcc and HCP metals, but due to their high stacking fault energies most studies on irradiated bcc metals have only observed perfect loops.[8,16,21,47,124] Since perfect loops are glissile, this can lead to more efficient sweeping up of radiation defects and accelerate the development of dislocation loop rafts or network dislocation structures in bcc materials. **Figure 16** shows examples of the dislocation loop microstructures in bcc, fcc, and HCP metals with similar atomic weight following electron irradiation at temperatures above recovery Stage III.[47] All of the loops are interstitial type with comparable size for the same irradiation dose. However, significant differences exist in the loop configurations, in particular habit planes and faulted (Ni, Zn) versus perfect (Fe) loops. One significant aspect of loop formation in HCP materials is that differential loop evolution on basal and prism planes can lead to significant anisotropic growth.[125–129]

In general, defect accumulation in the form of void swelling is significantly lower in bcc materials compared to fcc materials, although there are notable exceptions where very high swelling rates (approaching 3% per dpa)[130,131] have been observed in some bcc alloys. Pronounced elastic and point defect diffusion anisotropy[128] can also suppress void swelling in HCP materials, although high swelling has been observed in some HCP materials such as graphite.[132] It has long been recognized that ferritic/martensitic steels exhibit significantly lower void swelling than

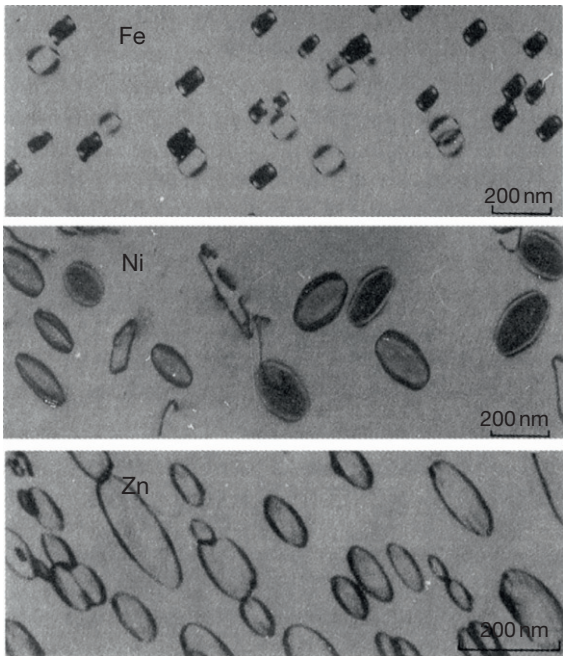

Figure 16 Dislocation loop microstructures in Fe, Ni, and Zn following electron irradiation at temperatures above recovery Stage III. The loops in Fe were perfect and located on (100) planes, and the loops in Ni and Zn were faulted and located on {111} and (0001) planes, respectively. Reproduced from Kiritani, M. *J. Nucl. Mater.* **2000**, *276*(1–3), 41–49.

austenitic stainless steels.[109,133,134] **Figure 17** compares the microstructure of austenitic stainless steel and 9%Cr ferritic/martensitic steel after dual beam ion irradiation at 650 °C to 50 dpa and 260 appm He.[135] Substantial void formation is evident in the Type 316 austenitic stainless steel, whereas cavity swelling is very limited in the 9%Cr ferritic/martensitic steel for the same irradiation conditions. Several mechanisms have been proposed to explain the lower swelling in ferritic/martensitic steel, including lower dislocation bias for SIA absorption, larger critical radii for conversion of helium bubbles to voids, and higher point defect sink strength.

1.03.3.6 Role of Atomic Bonding

Atomic bonding (i.e., metallic, ionic, covalent, and polar covalent) is a potential factor to consider when comparing the microstructural evolution between metals and nonmetals, or between different nonmetallic materials that may have varying amounts of directional covalent or ionic bonds. For example, several authors have proposed an empirical atomic bonding

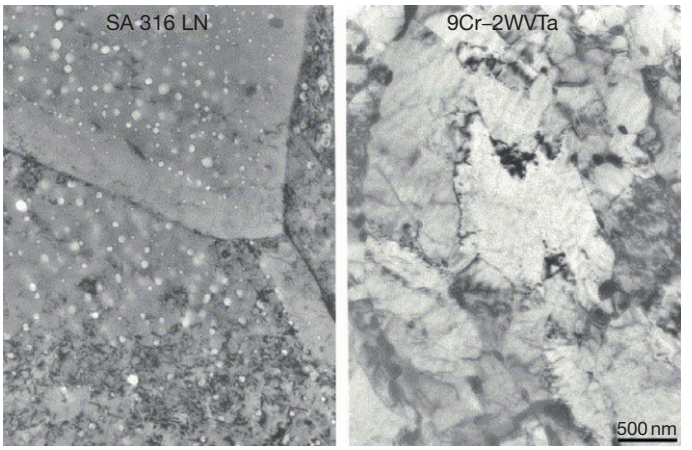

Figure 17 Comparison of the microstructure of Type 316 LN austenitic stainless steel and 9%Cr–2%WVTa ferritic/martensitic steel after dual beam ion irradiation at 650 °C to 50 dpa and 260 appm He. Reproduced from Kim, I.-S.; Hunn, J. D.; Hashimoto, N.; Larson, D. L.; Maziasz, P. J.; Miyahara, K.; Lee, E. H. *J. Nucl. Mater.* **2000**, *280*(3), 264–274.

criterion to correlate the amorphization susceptibility of nonmetallic materials.[136,137] Materials with ionicity parameters above 0.5 appear to have enhanced resistance to irradiation-induced amorphization. However, there are numerous materials which do not follow this correlation,[86,138,139] and a variety of alternative mechanisms have been proposed[86–88,138–141] to explain resistance to amorphization. Atomic bonding can directly or indirectly influence point defect migration and annihilation mechanisms (e.g., introduction of recombination barriers), and thereby influence the overall microstructural evolution.

1.03.3.7 Role of Dose Rate

The damage accumulation is independent of dose rate at very low temperatures, where point defect migration does not occur. However, at elevated temperatures (above recovery Stage I) the damage rate can have a significant influence on the damage accumulation. Simple elevated temperature kinetic models for defect accumulation[72,142–144] predict a transition from linear to square root dependence on the irradiation fluence when the radiation-induced defect cluster density becomes comparable to the density of preexisting point defect sinks such as line dislocations, precipitates, and grain boundaries. Similar square root flux dependence is predicted from more comprehensive kinetic rate theory models[6,70,71,145] for irradiation temperatures between recovery Stage II and IV. Electron microscopy analyses of electron[5] and neutron[146] irradiation experiments performed above recovery Stage I have reported defect cluster densities that exhibit square root dependence on irradiation flux or fluence.

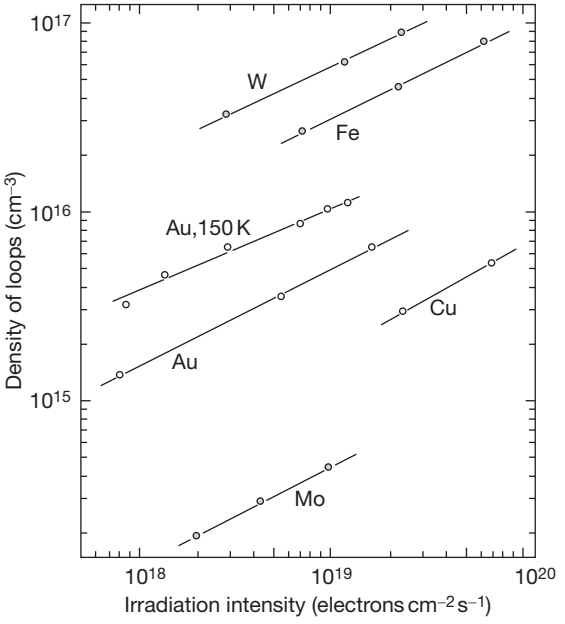

Figure 18 Effect of irradiation flux on the density of interstitial dislocation loops in several fcc and bcc metals during electron irradiation near room temperature or at cryogenic temperature (above recovery Stage I). Reproduced from Kiritani, M. In *Fundamental Aspects of Radiation Damage in Metals*, *CONF-751006-P2*; Robinson, M. T.; Young, F. W., Jr., Eds. National Tech. Inform. Service: Springfield, VA, 1975; Vol. II, pp 695–714.

Figure 18 summarizes the square root dose rate dependence for dislocation loop densities at intermediate temperatures in several electron-irradiated pure metals.[5]

Similarly, the predicted critical dose to achieve amorphization is independent of dose rate below

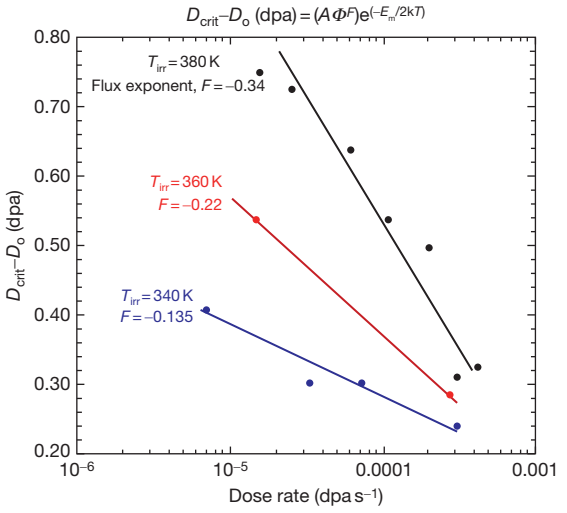

Figure 19 Effect of dose rate (Φ) on the critical dose (D_{crit}) to induce complete amorphization in 6H–SiC single crystals during 2 MeV Si ion irradiation. The dose D_0 corresponds to the amorphization dose at very low temperatures, where all defects are immobile. The equation at the top of the figure is the prediction from a model (ref. 147) for the dose dependence of amorphization on dose rate, point defect migration energy (E_m) and irradiation temperature (T). The parameter F describes the dose rate power law dependence and k is Boltzmann's constant. Based on data reported by Snead *et al.*[148]

recovery Stage I and depends on the inverse square root of dose rate for temperatures above recovery Stage I.[147] Experimental studies have confirmed that the threshold dose to achieve amorphization in ion-irradiated SiC is nearly independent of dose rate below ~350 K (corresponding to recovery Stage I) and approaches an inverse square root flux dependence for irradiation temperatures above 380 K, as shown in **Figure 19**.[148]

In the void swelling[149–151] and high temperature helium embrittlement[119,152,153] regimes, damage rate effects are very important considerations due to the competition between defect production and thermal annealing processes. Experimental studies using ion irradiation (~10^{-3} dpa s^{-1}) and neutron irradiation (~10^{-6} dpa s^{-1}) damage rates have observed that the peak void swelling regime is typically shifted to higher temperatures by about 100–150 °C for the high-dose rate irradiations compared to test reactor neutron irradiation conditions.[114,154–158] Similarly, the minimum and maximum temperature for measureable void swelling increase with increasing dose rate. For example, recent low dose rate neutron irradiation studies[111–113] performed near 10^{-9}–10^{-8} dpa s^{-1} have observed void swelling in austenitic stainless steel at temperatures as low as 280–300 °C, which is significantly lower than the ~400 °C lower limit for void swelling observed during fission reactor irradiations near 10^{-6} dpa s^{-1} (cf. **Figure 12**).

1.03.3.8 Role of Ionizing Radiation

Due to relatively large concentrations of conduction electrons, materials with metallic bonding typically do not exhibit sensitivity to ionizing radiation. On the other hand, semiconductor and insulating materials can be strongly affected by ionizing radiation by various mechanisms that lead to either enhanced or suppressed defect accumulation.[159] Some materials such as alkali halides, quartz, and organic materials, are susceptible to displacement damage from radiolysis reactions.[65,160–163] In materials that are not susceptible to radiolysis, significant effects from ionizing radiation can still occur via modifications in point defect migration behavior. Substantial reductions in point defect migration energies due to ionization effects have been predicted, and significant microstructural changes attributed to ionization effects have been observed in several semiconductors and inorganic insulator materials.[18,159,164–169] The effect of ionizing radiation can be particularly strong for electron or light ion beam irradiations of certain ceramic materials since the amount of ionization per unit displacement damage is high for these irradiation species; the ionization effect per dpa is typically less pronounced for heavy ion, neutron, or dual ion beam irradiation. **Figure 20** summarizes the effect of variations in the ratio of ionizing to displacive radiation (achieved by varying the ion beam mass) on the dislocation loops density and size in several oxide ceramics.[94,169,170] The loop density decreases rapidly when the ratio of ionizing to displacive radiation (depicted in **Figure 20** as electron-hole pairs per dpa) exceeds a material-dependent critical value, and the corresponding loop size simultaneously increases rapidly.

Numerous microstructural changes emerge in materials irradiated with so-called swift heavy ions that produce localized intense energy deposition in their ion tracks. Defect production along the ion tracks is observed above a material-dependent threshold value for the electronic stopping power with typical values of 1–50 keV nm^{-1}.[159,171–175] The microstructural changes are manifested in several ways, including dislocation loop punching,[176] creation of amorphous tracks with typical diameters of a few nm,[159,173,174,177–180] atomic disordering,[176,181,182] crystalline phase transformations,[171] destruction of preexisting small dislocation

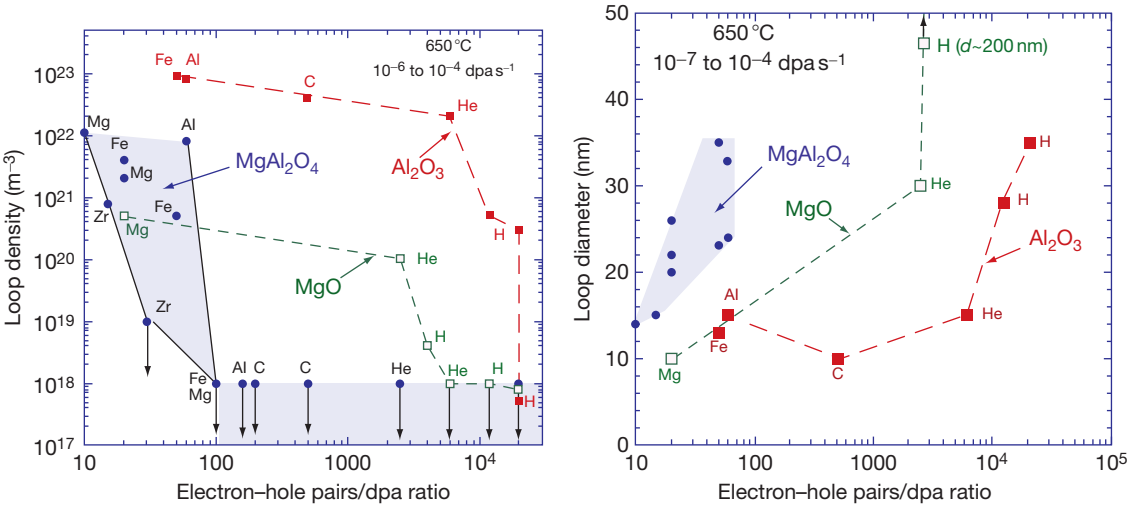

Figure 20 Effect of variations in ionizing to displacive radiation on the dislocation loop density and size in ion-irradiated MgO, Al_2O_3, and $MgAl_2O_4$. Adapted from Zinkle, S. J. *Radiat. Eff. Defects Solids* **1999**, *148*, 447–477; Zinkle, S. J. *J. Nucl. Mater.* **1995**, *219*, 113–127; Zinkle, S. J. In *Microstructure Evolution During Irradiation*; Robertson, I. M., Was, G. S., Hobbs, L. W., Diaz de la Rubia, T., Eds. Materials Research Society: Pittsburgh, PA, 1997; Vol. 439, pp 667–678.

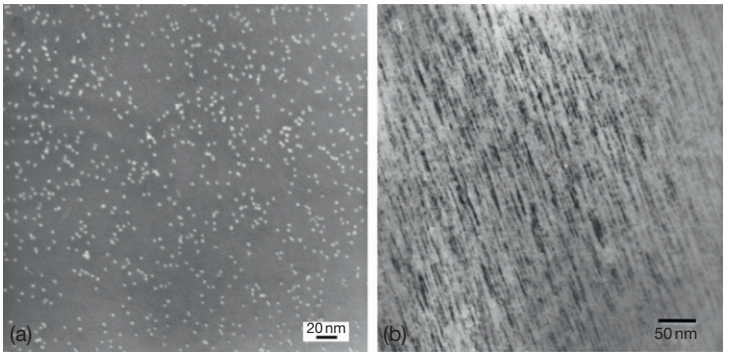

Figure 21 Plan view microstructure of disordered ion tracks in $MgAl_2O_4$ irradiated 430 MeV Kr ions at room temperature to a fluence of 6×10^{15} ions per square meter (isolated ion track regime) under (a) weak dynamical bright field and (b) $g = \langle 222 \rangle$ centered dark field imaging conditions (tilted 10° to facilitate viewing of the longitudinal aspects of the ion tracks). High-resolution TEM and diffraction analyses indicate disordering of octahedral cations (but no amorphization) within the individual ion tracks. Adapted from Zinkle, S. J.; Skuratov, V. A. *Nucl. Instrum. Methods B* **1998**, *141*(1–4), 737–746; Zinkle, S. J.; Matzke, H.; Skuratov, V. A. In *Microstructural Processes During Irradiation*; Zinkle, S. J., Lucas, G. E., Ewing, R. C., Williams, J. S., Eds. Materials Research Society: Warrendale, PA, 1999; Vol. 540, pp 299–304.

loops,[176] and formation of nanoscale hillocks and surrounding valleys[183,184] at free surfaces. Annealing of point defects occurs for irradiation conditions below the material-dependent threshold electronic stopping power for track creation,[159,180,185,186] whereas defect production occurs above the stopping power threshold.[159,171,173,175,178,180,183,185,186] The swift heavy ion annealing and defect production phenomena are observed in both metals and alloys[171,175,183,185,186] as well as nonmetals.[159,172,173,178–180,187–190] Defect production by swift heavy ions is of importance for understanding the radiation resistance of current and potential fission reactor fuel systems, including the mechanisms responsible for the finely polygonized rim effect[188,191] in UO_2 and radiation stability of inert matrix fuel forms.[182,189,191] The swift heavy ion defect production mechanism is generally attributed to thermal spike[178,192] and self-trapped exciton[187] effects. **Figure 21** shows examples of the plan view (i.e. along the direction of the ion beam) microstructure of disordered ion tracks in $MgAl_2O_4$ irradiated with swift heavy ions.[176,182]

1.03.3.9 Role of Solute Segregation and Precipitation

Solute atoms of importance include elements originally added to the material during fabrication and species produced by nuclear transmutation reactions (e.g., He and H, and a range of other elements). Solute atoms may exhibit preferential coupling with point defects created during irradiation, leading to either enhancement or depletion of solutes at point defect sink structures such as dislocations, grain boundaries, preexisting precipitates, and voids.[193–198] The solute-defect coupling can modify the kinetics for point defect diffusion, and the resultant solute enrichment or depletion may sufficiently modify the local composition to induce the formation of new phases. There are three general categories of precipitation associated with radiation-induced segregation processes[103,199]: radiation-induced (phases that form due to irradiation-induced nonequilibrium solute segregation and dissolve during postirradiation annealing), radiation-enhanced (precipitate formation accelerated or occurring at lower temperatures due to irradiation, but are thermally stable after formation), and radiation-modified (different chemical composition of precipitates compared to thermodynamically stable composition). In some materials, radiation-retarded precipitation (phase formation shifted to higher temperatures or longer exposure times) has been reported.[200]

A phenomenon that is uniquely associated with ion irradiation is the potential for the ions from the irradiating beam to modify the microstructural evolution by perturbing the relative balance of SIAs compared to vacancies flowing to defect sinks. The injected ions act as a source of additional interstitial atoms and can significantly suppress void nucleation and growth.[149,154,201,202] The peak concentration of the injected ions occurs near the displacement damage peak for ion irradiation, and therefore considerable care must be exercised when evaluating the void swelling data obtained near the peak damage region in ion-irradiated materials.[154,201,202] **Figure 22** shows an example of the dramatic changes in microstructure that can occur in the injected ion region.[203] In this example, void formation in ion-irradiated nickel at 400 °C is completely suppressed in the regions with the injected interstitials and the void microstructure is replaced with an aligned array of small interstitial-type dislocation loops.

Numerous studies have observed that the precipitation behavior during irradiation can strongly influence microstructural evolution, for example, the swelling behavior of austenitic stainless steels.[103,106,204–206]

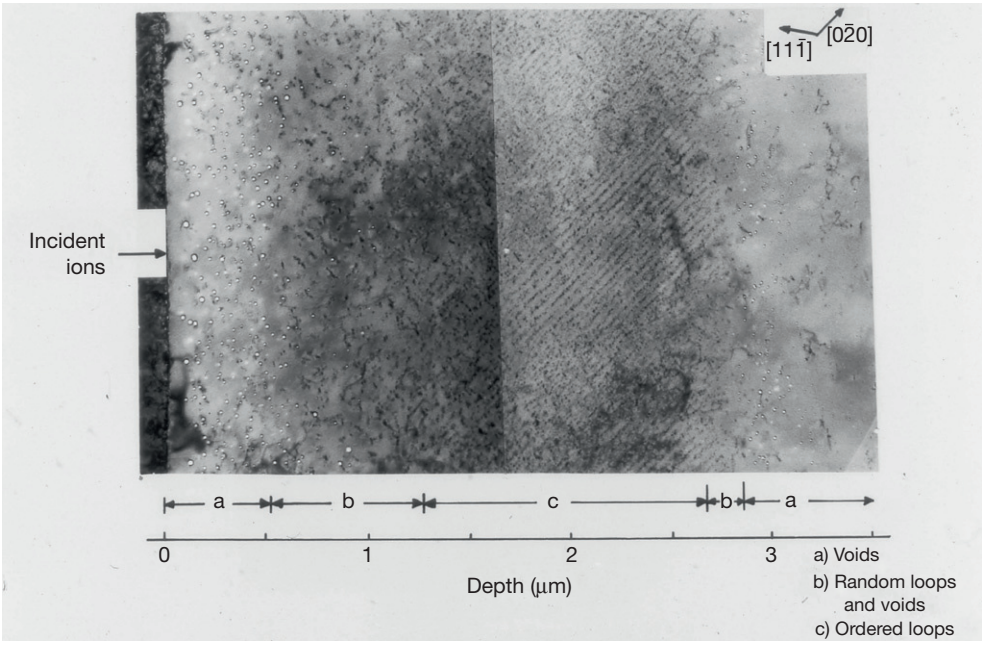

Figure 22 Cross-section TEM microstructure of nickel irradiated at 400 °C with 14 MeV Cu ions to a fluence of 5×10^{20} ions m^{-2} which produced a peak damage level of about 55 dpa at a depth near 2 μm. Void formation is completely suppressed in the injected interstitial regime (~1.3–2.8 μm) and the void microstructure is replaced with an array of small interstitial-type dislocation loops aligned along {100} planes. Reproduced from Whitley, J. B. Depth dependent damage in heavy ion irradiated nickel. University of Wisconsin, Madison, 1978.

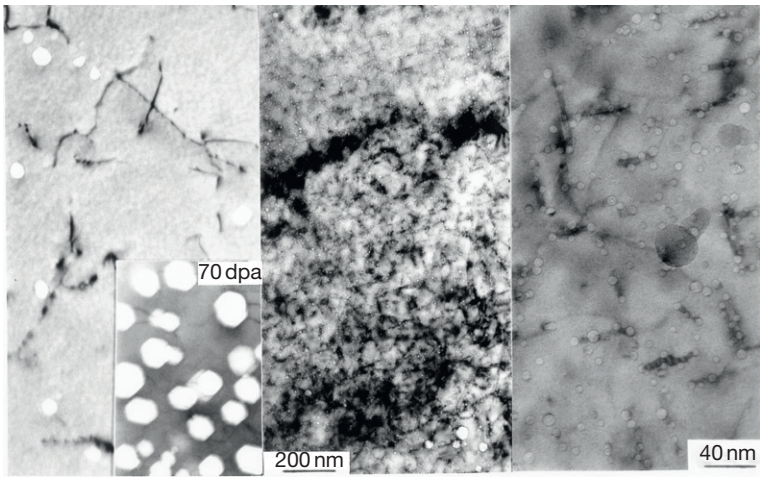

Figure 23 Comparison of the cavity microstructures for a pure Fe–13Cr–15Ni austenitic alloy (left panel) and the same alloy with P, Si, Ti, and C additions that produced dense radiation-induced phosphide precipitation (center and right panels) following dual beam Ni + He irradiation at 675 °C. The irradiation conditions were 0.4 dpa and 0.2 appm He for the left panel (70 dpa and 35 appm for the inset figure), and 109 dpa and 2000 appm He for the other two figures. Reproduced from Mansur, L. K.; Lee, E. H. *J. Nucl. Mater.* **1991**, *179–181*, 105–110.

In extreme cases, large-scale phase transformations can occur such as the γ (austenite, fcc) to α (ferritic, bcc) transformation in austenitic stainless steel following high dose neutron irradiation.[106,207] Depending on the type of precipitation, either enhanced or suppressed swelling can occur. Void swelling enhancement has generally been attributed to a point defect collector mechanism and typically occurs for moderate densities of relative coarse precipitates such as G phase in austenitic stainless steels, whereas void swelling suppression is generally observed for high densities of finely dispersed precipitates and is usually attributed to high sink strength effects.[103,151,208] **Figure 22** shows an example of the strong void swelling suppression associated with formation of radiation-induced Si- and Ti-rich phosphide precipitates compared to a simple Fe–Cr–Ni ternary austenitic alloy.[208] Similarly, the He/dpa ratio can influence the types and magnitude of point defect clusters and precipitation due to modifications in the point defect evolution under irradiation (**Figure 23**).[106]

1.03.4 Overview of Key Radiation-Induced Property Degradation Phenomena

There are eight major property changes that may occur in irradiated materials due to a variety of microstructural changes. Listed in order of increasing temperature where the effects are typically dominant, these phenomena are radiation-induced amorphization, radiation hardening (often accompanied by loss of tensile elongation and reduction in fracture toughness), decrease in thermal and electrical conductivity, mechanical property or corrosion degradation due to radiation-induced segregation and precipitation, dimensional instabilities due to three distinct phenomena (anisotropic irradiation growth, irradiation creep, void swelling), and high temperature embrittlement of grain boundaries due to helium accumulation. The microstructural origins associated with these eight degradation processes are summarized in the following sections, and more detailed descriptions of the property degradations in metals and nonmetals are given in accompanying chapters in this Comprehensive. The radiation doses at which these phenomena emerge to become of practical engineering significance are generally dependent on irradiation temperature, PKA energy, and material.

1.03.4.1 Radiation-Induced Amorphization

At very low temperatures where motion of SIAs or SIA clusters is limited, a crystalline to amorphous phase transition can be induced. The phase transition usually produces large swelling (5–30%) and decreases in elastic moduli.[15,91,182,209] This phase transition typically occurs for damage levels of ~0.1–1 dpa at low temperatures and has been attributed to several mechanisms including direct amorphization within collision cascades, and an increase in

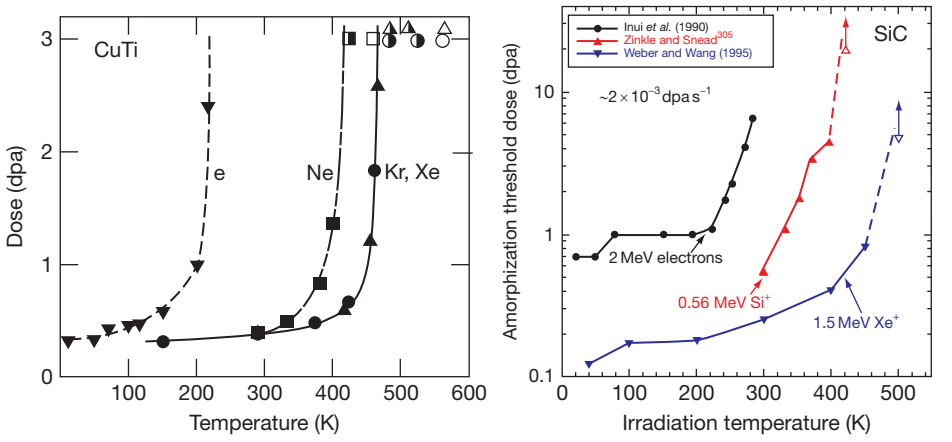

Figure 24 Effect of irradiating particle on the temperature-dependent dose for amorphization in irradiated CuTi[214] and SiC.[139] In both plots, filled symbols denote complete amorphization and open symbols denote amorphization did not occur.

the crystalline free energy due to point defect accumulation and disordering processes.[86,147,210–213] The dose dependence for accumulation of the amorphous volume fraction is significantly different for the direct impact mechanism compared to point defect accumulation or multiple overlap mechanisms.[213] As the irradiation temperature is raised to values where long range SIA and SIA cluster migration occurs, point defect diffusion to reduce the increase in free energy occurs and the dose to induce amorphization typically increases rapidly with increasing temperature until a temperature is reached where it is not possible to induce amorphization. In many cases, the critical temperature for amorphization increases with increasing PKA energy. **Figure 24** compares the effect of PKA energy on the temperature-dependent dose for complete amorphization for an intermetallic alloy[214] and a ceramic[139] material. In both materials, for all types of irradiating particles, the critical dose for amorphization increases rapidly when the irradiation temperature exceeds a critical value. The critical temperature for amorphization is significantly higher for heavy ion irradiation conditions compared to electron irradiation conditions.

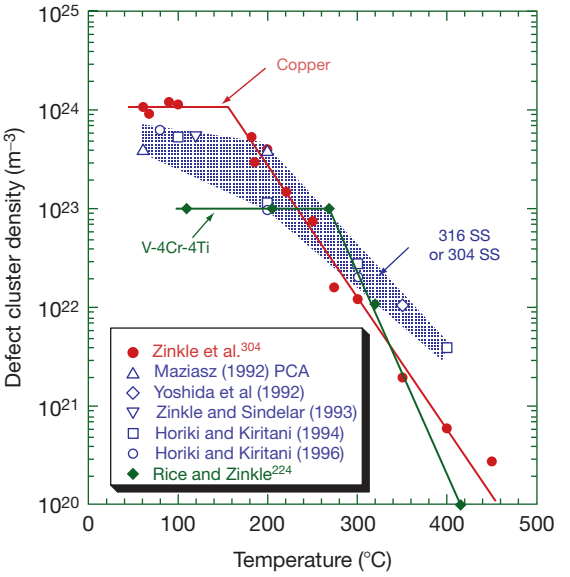

Figure 25 Comparison of the temperature-dependent defect cluster densities in neutron-irradiated Cu, austenitic stainless steel, and V–4Cr–4Ti. Based on data reported by Rice and Zinkle[224] and Rowcliffe *et al.*[225]

1.03.4.2 Radiation-Induced Hardening

Irradiation of metals and alloys at temperatures below recovery Stage V typically produces pronounced radiation hardening, as discussed in **Chapter 1.04, Effect of Radiation on Strength and Ductility of Metals and Alloys**. The matrix hardening is typically accompanied by reduction in tensile elongation and in many cases lower fracture toughness.[215–222] The uniform elongation measured in tensile tests for metals and alloys irradiated in this temperature regime usually decreases to <1% for damage levels above 0.1–1 dpa, which may require use of more conservative engineering design rules for the allowable stress of structural materials.[223] The hardening is largely due to the creation of high densities of sessile defect clusters, which act as obstacles to dislocation motion in the matrix. The defect cluster densities decrease rapidly with increasing temperature above recovery Stage V. **Figure 25** compares the temperature-dependent defect cluster densities[224,225]

observed in neutron-irradiated Cu, austenitic stainless steel, and V–4Cr–4Ti. Stage V annealing of defect clusters is evident for temperatures above ~150, ~200, and ~275 °C for Cu, stainless steel, and V–4Cr–4Ti, respectively. The mechanical properties in irradiated nonmetals at temperatures below recovery Stage V exhibit variable behavior, with observations of increased hardness,[226,227] unchanged strength,[228] and decreased hardness or flexural strength.[229–232]

1.03.4.3 Thermal and Electrical Conductivity Degradation

Thermal and electrical conductivity degradation can occur over a wide range of irradiation temperatures. For pure metals, there are two primary contributions: electron scattering from point defects (and associated defect clusters) and nuclear transmutation solute atoms. The conductivity degradation associated with radiation defects usually amounts to less than ~1% change except in the case of high void swelling conditions.[233–236] Conversely, the conductivity degradation associated with neutron-induced transmutation products tends to monotonically increase with increasing dose and typically becomes larger than the radiation defect contribution for doses above ~1 dpa. Thermal conductivity degradation much greater than 10% can occur in high-conductivity metals and ceramics.[235,237] The conductivity degradation in irradiated alloys can be complex due to short-range ordering and precipitation phenomena,[238] with the possibility for either increased or decreased conductivity compared to the unirradiated condition. For nonmetallic irradiated materials, the electrical conductivity during irradiation typically experiences a transient increase due to excitation of valence electrons into the valence band by ionizing radiation.[239–243] The thermal conductivity of irradiated nonmetals is typically degraded by displacement damage due to phonon scattering by point defects and defect clusters.[237,243–246]

1.03.4.4 Radiation-Induced Segregation and Precipitation

At intermediate temperatures where SIAs and vacancies are mobile, significant solute segregation to point defect sinks can occur. This can lead to precipitation of new phases due to the local enrichment or depletion of solute. These radiation-induced or -enhanced precipitation reactions typically become predominant phenomena in irradiated ferritic and austenitic steels at elevated temperatures for doses above about 10 dpa,[11,20,104,106,200,204] and in irradiated reactor pressure vessel steels at low dose rates for damage levels above 0.001–0.01 dpa.[247,248] Some general aspects of radiation-induced and -enhanced solute segregation and precipitation were described previously in **Section 1.03.3.9**. The solute segregation and precipitation associated with irradiation can lead to several deleterious effects including property degradation due to grain boundary or matrix embrittlement[224,247,249–252] and enhanced susceptibility for localized corrosion or stress corrosion cracking.[253–256] Solute segregation and precipitation can lead to either enhanced or suppressed void swelling behavior.[149,257,258] For austenitic stainless steel, undesirable precipitate phases that generally are associated with high void swelling include the radiation-induced phases $M_6Ni_{16}Si_7$ (G), Ni_3Si (γ'), MP, M_2P, and M_3P, and the radiation-modified phases M_6C, Laves, and M_2P.[200] The undesirable radiation-induced and -modified phases generally are associated with undersized misfits with the lattice, which tends to preferentially attract SIAs and thereby enhance the interstitial bias effect. **Figure 26** shows an example of enlarged cavity formation in association with G phase precipitates in neutron-irradiated austenitic stainless steel.[106] Potentially desirable radiation-enhanced and -modified phases (when present in the form of finely dispersed precipitates) include M_6C, Laves, $M_{23}C_6$, MC, σ, and χ.[200]

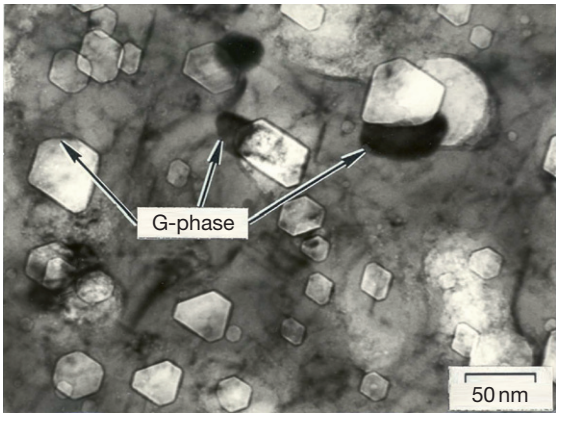

Figure 26 Enlarged cavity formation in association with G phase ($Mn_6Ni_{16}Si_7$) precipitates in Ti-modified 'prime candidate alloy' austenitic stainless steel following mixed-spectrum fission reactor irradiation at 500 °C to 11 dpa that generated 200 appm He. Reproduced from Maziasz, P. J. *J. Nucl. Mater.* **1989**, *169*, 95–115.

1.03.4.5 Dimensional Instabilities: Irradiation Growth, Creep, and Swelling

Irradiation growth (due to anisotropic nucleation and growth of dislocation loops on different habit planes) can be of significant practical concern at intermediate temperatures in anisotropic materials such as Zr alloys, Be, BeO, Al_2O_3, uranium, and graphite.[40,126,259–261] Anisotropic growth in individual grains in polycrystalline materials can produce large grain boundary stresses, leading to loss of strength and grain boundary fracture in some materials. **Figure 27** shows the large anisotropy in measured lattice parameter change in the basal and prism planes for BeO irradiated near room temperature.[262] For neutron fluences above 2×10^{20} cm^{-2} ($\sim$0.2 dpa) with a *c*-axis expansion $>$0.5% and an *a*-axis expansion near 0.1%, a rapid decrease in flexural strength was observed.[262,263] In materials with highly textured grains, unacceptable anisotropic growth at the macroscopic level can occur. One engineering solution is to use processing techniques to produce randomly aligned, small grain-sized materials.

Irradiation creep occurs in the presence of applied stress, due to biased absorption of point defects at cavities and along specific dislocation orientations relative to the applied stress.[264] Irradiation creep produces dimensional expansion that acts in addition to normal thermal creep mechanisms and is most prominent at temperatures from recovery Stage III up to temperatures where thermal creep deformation becomes rapid (typically above 0.5 T_M). The magnitude of steady-state irradiation creep is proportional to the applied stress level and dose, and consists of a creep compliance term and a void swelling term. The magnitude of typical irradiation creep compliance coefficients[260,265,266] for fcc and bcc metals is $0.5–1 \times 10^{-12}$ Pa^{-1} dpa^{-1}. The irradiation creep compliance for ferritic/martensitic steels appears to be about one-half of that for austenitic steels.[109] Accelerated irradiation creep due to differential absorption of point defects at low temperatures (e.g. below recovery Stage V) or at low doses can produce creep deformation rates that are up to 10–100 times larger than the steady-state irradiation creep rates.[267,268]

Volumetric swelling from void formation occurs at temperatures above recovery Stage V in fcc and HCP materials (and above Stage III for bcc materials), and typically exhibits a linear increase with dose after an initial transient regime. As summarized in **Figure 28** the dose-dependent swelling in fast fission reactor-irradiated austenitic stainless steel progresses

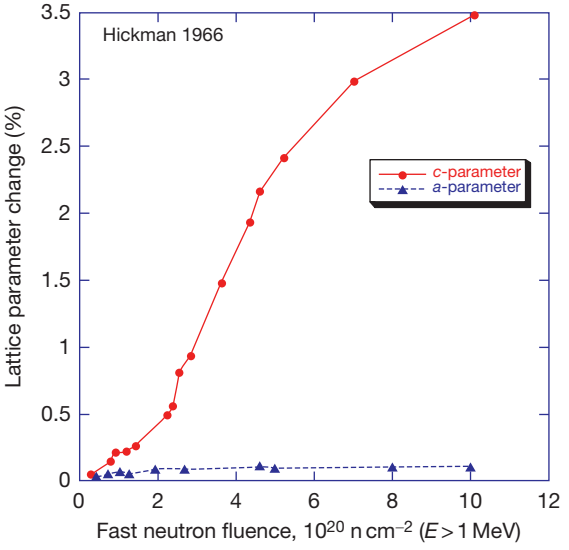

Figure 27 Effect of fission neutron irradiation near 75 °C on the measured lattice parameter changes for BeO. Adapted from Hickman, B. S. In *Studies in Radiation Effects, Series A: Physical and Chemical*; Dienes, G. J., Ed. Gordon and Breach: New York, 1966; Vol. 1, pp 72–158.

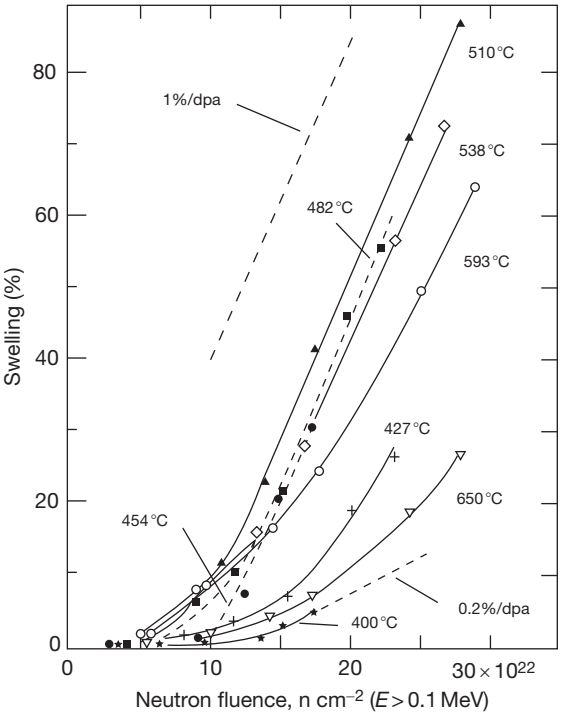

Figure 28 Summary of dose-dependent swelling behavior in 20% cold-worked Type 316 austenitic stainless steel due to fast fission reactor irradiation. Reproduced from Garner, F. A.; Toloczko, M. B.; Sencer, B. H. *J. Nucl. Mater.* **2000**, *276*, 123–142.

at a swelling rate of ~1%/dpa without evidence for saturation up to swelling levels approaching 100%.[109] Similar high swelling levels without evidence of saturation have been observed in pure copper[108] and some simple bcc alloys.[131] Volumetric swelling levels in structural materials in excess of ~5% are difficult to accommodate by engineering design,[269] and additional embrittlement mechanisms may appear in austenitic stainless steel for swelling levels above 10% including void channeling and loss of ductility.[270,271] Therefore, there is strong motivation to design structural materials that are resistant to void swelling by introducing a high matrix density of point defect sinks or other techniques. In general, the amount of void swelling is lower in bcc materials compared to fcc materials.[50,92,109] For example, the observed void swelling in many ferritic/martensitic steels is <2% after fission neutron damage levels of 50 dpa or higher, whereas the void swelling in simple austenitic stainless steels may be 30% or higher.[109] The superior swelling resistance in ferritic/martensitic steels is largely due to a higher transient dose before onset of steady-state swelling, along with a lower steady-state swelling rate. For many HCP materials, the amount of void swelling is relatively small compared to fcc materials due to anisotropic point defect migration that tends to promote defect recombination.[128] However, the potential for anisotropic swelling associated with cavity formation in HCP materials may induce large stresses and potential cracking at grain boundaries.[263,272,273] **Figure 29** shows an example of aligned cavity formation and grain boundary separation in Al_2O_3 following fast fission reactor irradiation.[272]

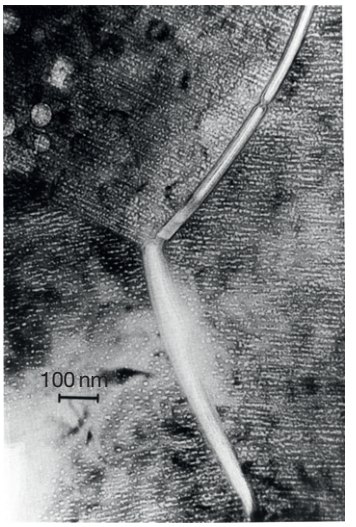

Figure 29 Aligned cavity formation and grain boundary separation in Al_2O_3 following fast fission reactor irradiation to 12 dpa at 1100 K. Reproduced from Clinard, F. W., Jr.; Hurley, G. F.; Hobbs, L. W. *J. Nucl. Mater.* **1982**, *108–109*, 655–670.

1.03.4.6 High Temperature Embrittlement

High temperature helium embrittlement occurs at elevated temperatures (typically near or above $0.5\,T_M$) when sufficient levels of helium are produced by nuclear transmutation reactions and mechanical stress is applied during irradiation. Intergranular fracture is induced by the transformation of grain boundary bubbles to voids, leading to breakaway growth, cavity coalescence, and rupture in the presence of mechanical stress.[120,152,153,274–277] The application of tensile stress during high temperature irradiation induces migration of the helium to the grain boundaries, where large cavities can be formed.[120] In the absence of applied stress, the helium bubbles are distributed throughout the material. The observed tensile ductility due to helium embrittlement decreases with decreasing strain rate[120,278] and decreasing stress[120] (opposite of the behavior observed in many unirradiated metals and alloys), pointing out the importance of exposure time at elevated temperature on helium embrittlement. **Figure 30** shows examples of the grain boundary microstructures of an Fe–Cr–Ni ternary alloy preimplanted with 160 appm He during annealing at 750 °C with and without applied tensile stress.[279] Cavity formation along the grain boundary is very limited in the absence of applied stress for annealing times up to 60 h, whereas pronounced grain boundary cavity swelling occurs for annealing times as short as 8 h when ~20 MPa stress is applied. Evidence for high temperature helium embrittlement has been observed during tensile and creep testing of austenitic stainless steel at temperatures above 550 °C (~$0.45–0.5\,T_M$) when the helium concentration exceeds ~30 appm.[255,265,277,280,281] Austenitic stainless steels containing fine dispersions of precipitates exhibit better resistance to helium embrittlement than simple Fe–Cr–Ni alloys, and microstructural investigations suggest that helium trapping at grain interior locations (thereby impeding the flow of helium to grain boundaries) is an important factor.[152,277,282–284] It has been observed that ferritic/martensitic steels exhibit better resistance to grain boundary helium cavity formation and growth compared to austenitic stainless steels.[274,285–287] This has been attributed to several potential factors, including efficient trapping

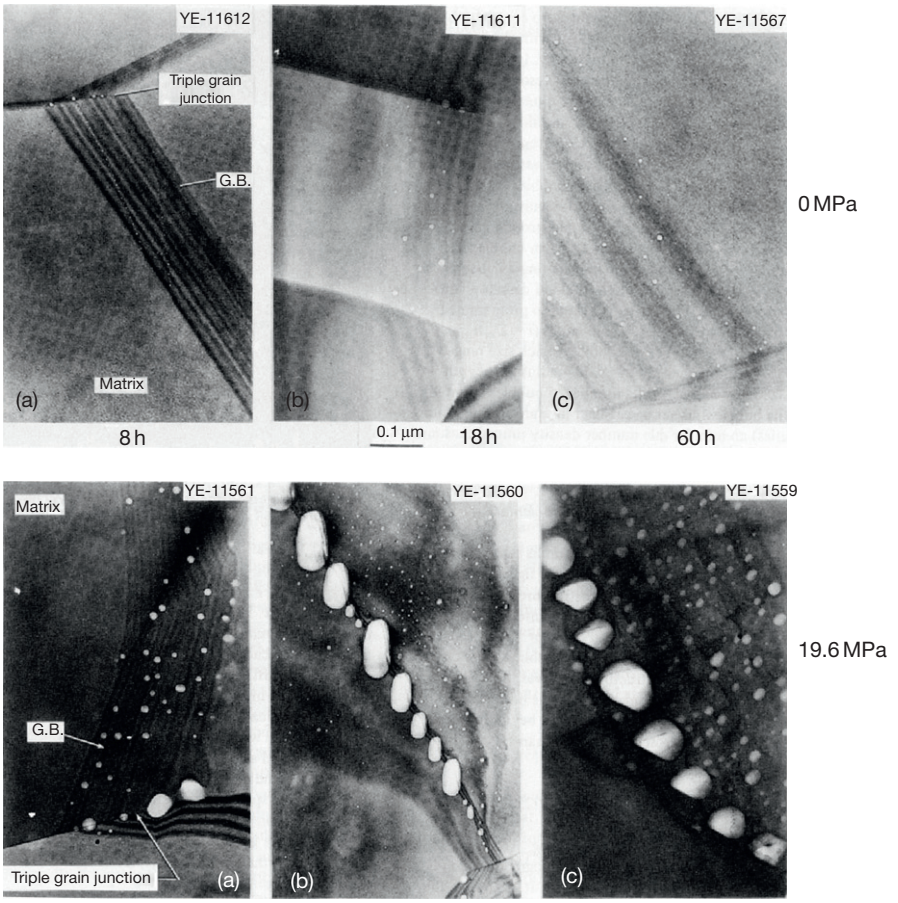

Figure 30 Effect of exposure time and applied stress during annealing at 750 °C on the formation of grain boundary cavities in Fe–17Cr–17Ni austenitic alloy preimplanted with 160 appm helium. Reproduced from Braski, D. N.; Schroeder, H.; Ullmaier, H. *J. Nucl. Mater.* **1979**, *83*, 265–277.

of helium in the ferritic steel grain interior by precipitates and other features, a potentially larger critical radius for conversion of helium bubbles to voids in ferritic steel, and lower matrix strength for ferritic steel compared to austenitic steel.[119,274,286,288] The helium bubble densities observed in model Fe–Cr ferritic alloys and commercial ferritic steels following high temperature implantation are comparable to that observed in austenitic steels.[118] Relatively good resistance to helium embrittlement compared to austenitic stainless steel has been observed in other bcc metals such as Nb and Nb–1Zr (no severe embrittlement observed for He concentrations up to 100–500 appm),[289–291] whereas simple fcc metals such as pure copper are readily susceptible to helium embrittlement even at relatively high (tensile) strain rates at temperatures near $0.5\,T_M$ for He concentrations of 100–330 appm.[292,293]

1.03.5 Examples of Radiation-Induced Microstructural Changes

1.03.5.1 Dislocation Loop Formation

A common feature in many irradiated metals and nonmetals at temperatures between recovery Stage III and Stage V is dislocation loop formation (either perfect or faulted), with typical loop diameters ranging from ~2 to ~100 nm. Both vacancy (intrinsic) and interstitial (extrinsic) loops are frequently observed in irradiated materials. The dislocation loop shape is frequently circular (in order to minimize dislocation line length), but rhombus, square, hexagonal, or other shapes have been observed in some materials due to elastic energy considerations.[21] **Figure 31** shows an example of circular faulted interstitial-type dislocation loop formation in $MgAl_2O_4$ due to ion irradiation at 650 °C. The parallel fringes visible in the loop

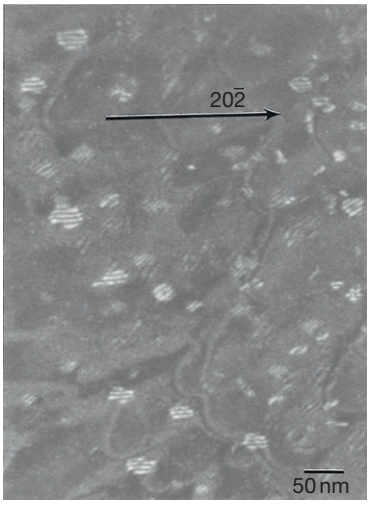

Figure 31 Faulted interstitial-type dislocation loop formation in $MgAl_2O_4$ irradiated with 2 MeV Al^+ ions at 650 °C to 14 dpa. The image was taken with a beam direction near [101] using weak beam dark field (*g*, 6*g*), $g = 20\bar{2}$ diffraction imaging conditions (data from S. J. Zinkle, unpublished research).

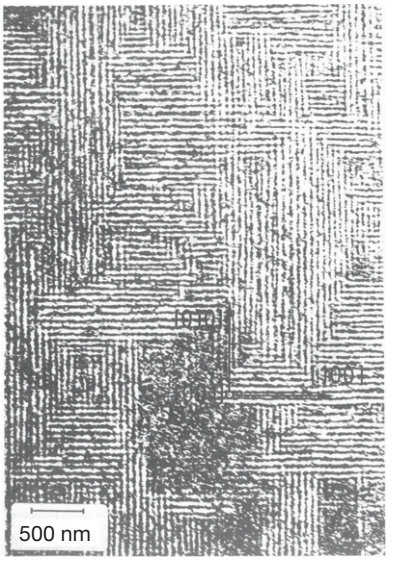

Figure 32 Defect cluster patterning into aligned {001} walls in single crystal copper irradiated with protons at 100 °C to 2 dpa. Reproduced from Jäger, W.; Trinkaus, H. *J. Nucl. Mater.* **1993**, *205*, 394–410.

interiors are a signature of the stacking fault and are visible in TEM by selecting the appropriate diffraction imaging conditions. Faulted loop formation is energetically unfavorable in most bcc materials due to their high stacking fault energies, although there is some evidence for formation of small faulted loops in some cases.[224] Experimental studies using energetic ion beams at cryogenic temperatures (where long range point defect migration does not occur) have obtained convincing evidence for direct formation of visible defect clusters directly within displacement cascades above a threshold energy value.[294] Dislocation loop formation is usually randomly distributed on the relevant habit planes, with no pronounced spatial correlation. In some cases where mechanical or radiation-induced stresses are present, significant anisotropy occurs regarding the habit planes for loop formation.[295,296] Within a limited temperature and damage rate regime, the dislocation loop microstructure in some materials also exhibits a tendency to self-organize into aligned walls.[297–299] Figure 32 shows an example of well-developed defect cluster patterning in pure copper following proton irradiation to 2 dpa.[298] The defect clusters within the walls consist of SFTs and small dislocation loops.

1.03.5.2 Network Dislocation Formation

Network dislocation structures are routinely observed in metals[5,8,200] and ceramics[300,301] irradiated at temperatures above recovery Stage I to temperatures in excess of recovery Stage V. During prolonged irradiation, the microstructural evolution typically involves formation and growth of faulted dislocation loops, loop unfaulting to create perfect dislocation loops, and then loop interaction/impingement to form network dislocation structures. The network dislocations are typically randomly distributed and are often heavily jogged as opposed to the relatively straight dislocations found in unirradiated metals. Figure 33 shows a typical network dislocation microstructure for irradiated copper.[302] The quantitative value of the dislocation density can vary significantly among different materials within the same crystal structure. For example, typical network dislocation densities in irradiated metals at temperatures between recovery Stages III and V range from ~0.01 to ~0.1×10^{14} m^{-2} for Cu[302–304] to ~$1–10 \times 10^{14}$ m^{-2} for pure Ni[304] and austenitic stainless steel.[20]

1.03.5.3 Stacking Fault Tetrahedra

Irradiation of fcc metals under energetic displacement cascade conditions induces the formation of stacking fault tetrahedra. Figure 34 shows an example of the formation of small dislocation loops and SFTs (triangle-shaped projected images) in copper due to irradiation with 750 MeV protons (2.5 MeV average PKA energy) at ~90 °C to ~0.7 dpa.[302]

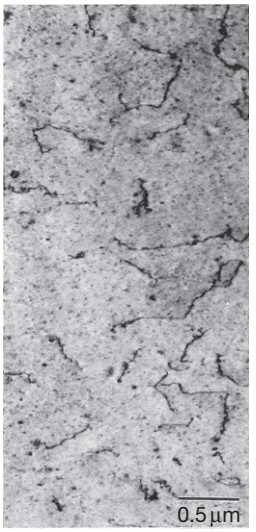

Figure 33 Dislocation microstructure of pure copper following irradiation with 750 MeV protons at ~200 °C to ~2 dpa. Reproduced from Zinkle, S. J.; Horsewell, A.; Singh, B. N.; Sommer, W. F. *J. Nucl. Mater.* **1994**, *212–215*, 132–138.

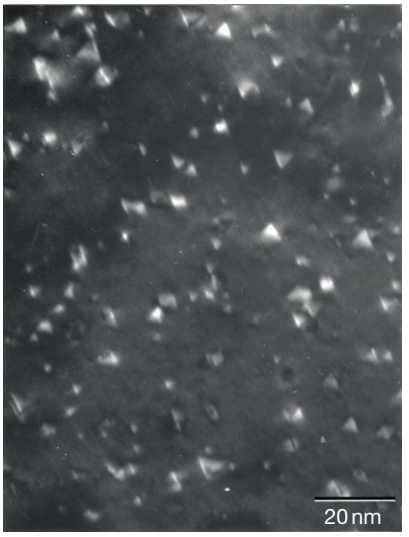

Figure 34 Weak beam dark field (g, $4g$), $g = 002$ microstructure of pure copper following irradiation with 750 MeV protons at ~90 °C to ~0.7 dpa. The TEM figure is based on irradiated specimens described in Zinkle *et al.*[302] The SFTs are visible as small triangle-shaped defects since the electron beam direction was near [110] (data from S. J. Zinkle, unpublished research).

The SFTs are thermally stable up to recovery Stage V. SFTs have been observed in numerous irradiated fcc metals, including aluminum,[305] copper,[12,53,146,302,306,307] nickel,[304,307–309] silver,[306,307] gold,[307,310,311] palladium,[310,312] and austenitic stainless steels.[53,96,307,312,313] Evidence from thin film and low-dose irradiation studies using ion beams or other energetic displacement cascade conditions suggests that SFTs can be formed directly in displacement cascades when the PKA energy exceeds a threshold value of ~5–10 keV, in agreement with molecular dynamics simulations.[26,29] There are also several observations of SFT formation in some fcc metals due to point defect nucleation and growth during electron irradiation.[299,305] The results from irradiations performed under energetic displacement cascade conditions at temperatures near recovery Stage I suggest that SFTs are not visible, perhaps due to insufficient rearrangement of the vacancy-rich core within the rapidly quenched displacement cascade.[74,305]

1.03.5.4 Dislocation Channeling and Flow Localization

Mechanical deformation of metals and alloys after irradiation at temperatures below recovery Stage V produces deformation microstructures that typically evolve from predominantly dislocation cell microstructures in the unirradiated and low-dose irradiated conditions to a variety of localized deformation microstructures above a threshold damage level including twinning, planar dislocation deformation, and formation of dislocation channels.[314–316] Formation of cleared dislocation channels has been suggested to be the cause of low uniform elongations observed in tensile tests of metals and alloys irradiated at temperatures below recovery Stage V,[221,317] and dislocation channeling is frequently observed following deformation of irradiated materials that exhibit low uniform elongation.[95,96,100,312,316,318–321] An alternative mechanism for the low uniform elongations in irradiated materials, based on a material-specific threshold stress for plastic instability, has also been proposed.[216,322–324] The spacing between dislocation channels is typically on the order of 1 µm, and the width of the individual channels ranges from ~20 to 200 nm. Localized deformation visible as surface slip steps in irradiated copper following tensile straining has been directly correlated with cleared dislocation channels.[325] The matrix regions between the cleared channels do not exhibit evidence of substantial dislocation activity, suggesting that all of the dislocation motion associated with deformation is restricted to the dislocation channel regions. **Figure 35** shows an example of cleared dislocation channels observed in austenitic stainless steel following fission neutron

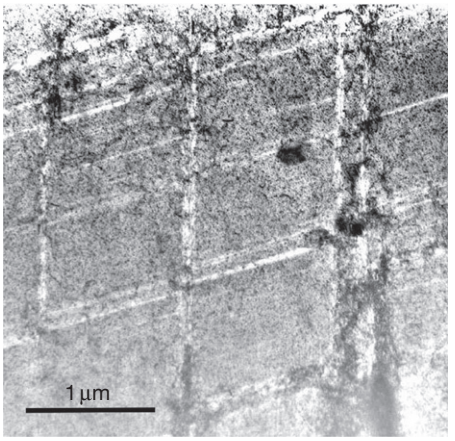

Figure 35 Cleared dislocation channels observed in Type 316 austenitic stainless steel following fission neutron irradiation to 0.78 dpa near 80 °C and subsequent uniaxial tensile deformation to 32% strain. The electron beam direction was near [110]. Reproduced from Byun, T. S.; Hashimoto, N.; Farrell, K.; Lee, E. H. *J. Nucl. Mater.* **2006**, *349*, 251–264.

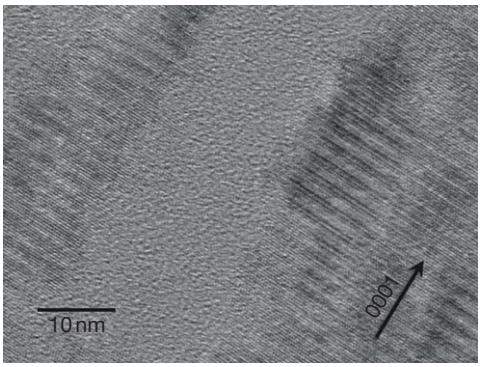

Figure 36 High-resolution transmission electron microscopy image of single crystal 6H–SiC following 0.56 MeV Si ion irradiation at 60 °C to a damage level of ~2.6 dpa. Reproduced from Snead, L. L.; Zinkle, S. J.; Hay, J. C.; Osborne, M. C. *Nucl. Instrum. Methods B* **1998**, *141*, 123–132.

irradiation to 0.78 dpa near 80 °C and subsequent uniaxial tensile deformation to 32% strain.[326]

The mechanisms responsible for annihilation of SFTs by gliding dislocations within the dislocation channel include stress-induced collapse to triangle loops, multiple shear, partial annihilation with a remnant apex, collapse to a triangle loop or complete annihilation with multiple super jogs, and complete annihilation by screw dislocations followed by cross slip.[327–329] Computer simulations of dislocation loop interactions with gliding dislocations suggest multiple potential mechanisms that could lead to defect-cleared dislocation channels, including absorption, unfaulting, and shear of the loops.[330–333] Detailed experimental confirmation of these annihilation mechanisms is still needed.

1.03.5.5 Crystalline to Amorphous Phase Transitions

Radiation-induced amorphization can proceed by several different mechanisms, including direct impact amorphization and gradual accumulation of lattice defects and chemical disorder that eventually causes destabilization of the crystalline matrix.[213] Figure 36 shows an example of the microstructure near the crystalline to amorphous transition dose in ion-irradiated SiC, where the amorphization is induced by gradual buildup of radiation defects.[209]

At intermediate doses, amorphous islands gradually emerge from the initially crystalline matrix in SiC irradiated at low temperatures. Direct amorphization within individual displacement cascades has been observed in several intermetallic,[334] semiconductor,[12,335] and ceramic insulator[15,336,337] materials. In many other materials, extensive chemical disordering from displacement cascades or point defects precedes amorphization.[3,76,87] The chemical disordering can be monitored either on the nanoscale dimensions (e.g., due to individual displacement cascades) by techniques such as transmission electron microscopy,[12,338] or an integrated average value by various techniques including X-ray diffraction, TEM, and Rutherford backscattering spectrometry.[76,339] As previously noted in Section 1.03.3.8, the intense ionization associated with swift heavy irradiation can lead to amorphization either directly within ion tracks, or by a cumulative process involving chemical disordering before amorphization due to multiple overlapping ion tracks.

1.03.5.6 Radiation-Induced Precipitation

As previously outlined in Sections 1.03.3.9 and 1.03.4, phase changes associated with irradiation can be manifested in a variety of geometries, including randomly distributed matrix or grain boundary precipitates, continuous grain boundary films, precipitate-free zones near grain boundaries or other point defect sinks, spatially ordered arrays of precipitates, large-scale (>100 nm) phase transformations, and

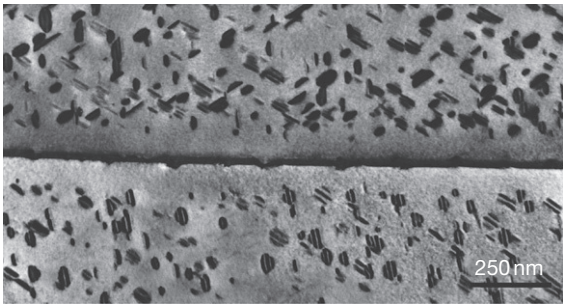

Figure 37 Radiation-induced precipitates on {001} habit planes observed next to a grain boundary in V–4Cr–4Ti following neutron irradiation to 0.1 dpa at 505 °C. The fringe contrast in the precipitate interior is due to the $a/3\langle 001\rangle$ displacement vector of the precipitates relative to the vanadium alloy matrix. The beam direction was {111} and the diffraction vector was $g = 01\bar{1}$. Reproduced from Rice, P. M.; Zinkle, S. J. *J. Nucl. Mater.* **1998**, *258–263*, 1414–1419.

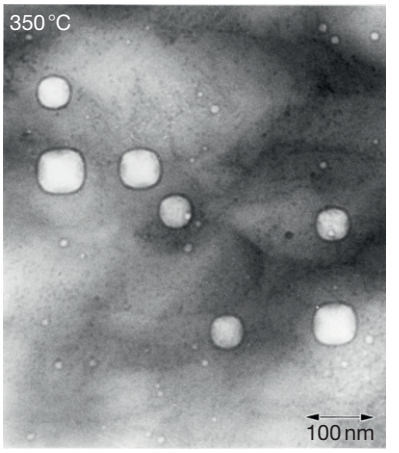

Figure 38 Voids and small helium-filled bubbles in a copper–boron alloy following fission neutron irradiation to 1.2 dpa at 350 °C. Reproduced from Zinkle, S. J.; Farrell, K.; Kanazawa, H. *J. Nucl. Mater.* **1991**, *179–181*, 994–997.

dissolution or growth of thermally stable precipitates. Preferential coupling of solute atoms to point defect fluxes can lead to modifications in the chemistry of precipitates as well as nucleation of phases that would not be stable under thermal equilibrium conditions. Figure 37 shows an example of radiation-induced platelet precipitates observed in the grain interiors of V–4Cr–4Ti following neutron irradiation to 0.1 dpa at 505 °C.[224] A precipitate-free zone is observed adjacent to the grain boundary in this figure.

1.03.5.7 Cavity Formation

Several different cavity geometries are created in irradiated materials. For helium-filled bubbles, the cavity shape is typically spherical. For voids, faceted cavities with faces corresponding to low-index crystallographic planes are often created, e.g. truncated {111} octahedra or {001} cubes in fcc materials, truncated {110} dodecahedra or {001} cubes in bcc materials, and more complex shapes in HCP materials,[21,22,340–342] although nearly spherical shapes are also sometimes observed for voids. When helium is generated during irradiation (due to neutron-induced transmutation reactions, etc.), a bimodal cavity distribution is usually observed with the small cavities corresponding to helium-filled bubbles and the large cavities corresponding to underpressurized voids. The critical radius transition between bubbles and voids is determined by a balance between dislocation bias-induced vacancy influx and pressure-modified thermal emission of vacancies.[120,151,208,274,343] Figure 38 shows an example of large faceted voids and small helium-filled spherical bubbles in a neutron-irradiated copper–boron alloy.[107] The visible cavity density usually increases rapidly at low doses, and approaches a constant value for damage levels above ~1–50 dpa. The void size tends to increase continuously with increasing dose.

Well-developed periodic void lattices have been observed in several irradiated materials.[297,344,345] Void lattice formation has most frequently been observed in bcc materials, but periodically aligned void structures have also been observed in HCP[272,346,347] and fcc[303,348–351] materials. Aligned voids have been observed in both metals and ceramic insulators. The aligned cavities in HCP materials are usually manifested as one- or two-dimensional arrays perpendicular or parallel to the basal plane, respectively.[297,346] The void lattices in bcc and fcc materials adopts the same three-dimensional crystallographic symmetry as the host lattice.[297] The swelling levels in bcc metals with well-developed void lattices are typically a few percent, which has led to hypotheses that void lattice formation may coincide with a cessation in steady-state swelling.[117,352] The saturation in void swelling is associated with achieving a constant average void size. Figure 39 shows an example of a well-developed bcc void lattice in ion-irradiated Nb–1Zr.[353] In the study by Loomis *et al.* it was reported that void lattice formation did not occur unless a threshold level of oxygen was present (60–2700 appm oxygen, depending on the irradiated material).

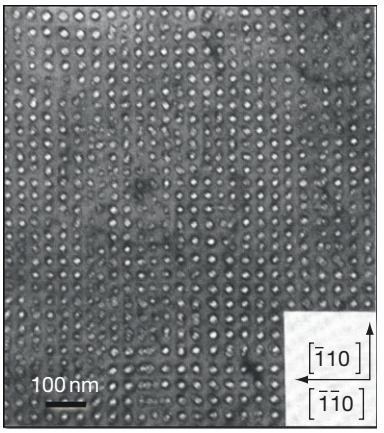

Figure 39 Void lattice formation in Nb–1Zr containing 2700 appm oxygen following irradiation with 3.1 MeV V^+ ions to 50 dpa at 780 °C. Reproduced from Loomis, B. A.; Gerber, S. B.; Taylor, A. *J. Nucl. Mater.* **1977**, *68*, 19–31.

1.03.6 Summary

Radiation-induced microstructural modifications can create large changes in the physical and mechanical properties of materials, as detailed in accompanying chapters in this book. The two most important extrinsic variables that influence microstructural evolution under irradiation are the radiation damage level and temperature. Many similarities are observed for diverse materials and irradiation spectra if the comparisons are performed at comparable damage levels and defect mobility regimes (defect recovery stages). The PKA energy often exerts a significant influence on the microstructural evolution, in particular by inducing direct cascade amorphization or creation of defect clusters within displacement cascades when the PKA energy exceeds a threshold energy value. Numerous other parameters such as dose rate, crystal structure, and atomic weight typically exert less pronounced influence on microstructural evolution, although very large qualitative and quantitative effects can be observed under some circumstances.

Acknowledgments

Much of the author's work discussed in this chapter was sponsored by the U.S. Department of Energy, Office of Fusion Energy Sciences.

References

1. Zinkle, S. J.; Ice, G. E.; Miller, M. K.; Pennycook, S. J.; Wang, X.-L. *J. Nucl. Mater.* **2009**, *386–388*, 8–14.
2. Zhang, Y.; Weber, W. J.; Jiang, W.; Hallen, A.; Possnert, G. *J. Appl. Phys.* **2002**, *91*(10), 6388–6395.
3. Kinoshita, C. *J. Electron Microsc.* **1985**, *34*(4), 299–310.
4. Kinoshita, C. *J. Nucl. Mater.* **1992**, *191–194*, 67–74.
5. Kiritani, M. In *Fundamental Aspects of Radiation Damage in Metals, CONF-751006-P2*, Robinson, M. T., Young, F. W., Jr., Eds. National Tech. Inform. Service: Springfield, VA, 1975; Vol. II, pp 695–714.
6. Kiritani, M.; Yoshida, N.; Takata, H.; Maehara, Y. *J. Phys. Soc. Jpn.* **1975**, *38*(6), 1677–1686.
7. English, C. A. *J. Nucl. Mater.* **1982**, *108–109*, 104–123.
8. Eyre, B. L. *J. Phys. F* **1973**, *3*(2), 422–470.
9. Eyre, B. L. In *Fundamental Aspects of Radiation Damage in Metals, CONF-751006-P2*, Robinson, M. T., Young, F. W., Jr., Eds. National Tech. Inform. Service: Springfield, VA, 1975; Vol. II, pp 729–763.
10. Farrell, K. *Radiat. Effects* **1980**, *53*, 175–194.
11. Gelles, D. S. In *Reduced Activation Materials for Fusion Reactors*, Klueh, R. L., Gelles, D. S., Okada, M., Packan, N. H., Eds. American Society for Testing and Materials: Philadelphia, PA, 1990; pp 113–129.
12. Kiritani, M. *J. Nucl. Mater.* **1986**, *137*, 261–278.
13. Kiritani, M., Recoil energy effects and defect processes in neutron irradiated metals. *J. Nucl. Mater.* **1988**, *155–157*, 113–120.
14. Kiritani, M., Defect interaction processes controlling the accumulation of defects produced by high energy recoils. *J. Nucl. Mater.* **1997**, *251*, 237–251.
15. Weber, W. J.; Ewing, R. C.; Catlow, C. R. A.; *et al. J. Mater. Res.* **1998**, *13*(6), 1434–1484.
16. Wilkens, M. In *Vacancies and Interstitials in Metals*; Seeger, A., Schumacher, D., Schilling, W., Diehl, J., Eds. North-Holland: Amsterdam, 1970; pp 485–529.
17. Zinkle, S. J. *Nucl. Instrum. Methods B* **1994**, *91*, 234–246.
18. Zinkle, S. J.; Kinoshita, C. *J. Nucl. Mater.* **1997**, *251*, 200–217.
19. Zinkle, S. J.; Matsukawa, Y. *J. Nucl. Mater.* **2004**, *329–333*, 88–96.
20. Zinkle, S. J.; Maziasz, P. J.; Stoller, R. E. *J. Nucl. Mater.* **1993**, *206*, 266–286.
21. Smallman, R. E.; Westmacott, K. H. *Mater. Sci. Eng.* **1972**, *9*(5), 249–272.
22. Zinkle, S. J.; Seitzman, L. E.; Wolfer, W. G. *Philos. Mag. A* **1987**, *55*(1), 111–125.
23. Bacon, D. J.; Gao, F.; Osetsky, Y. N. *J. Nucl. Mater.* **2000**, *276*, 1–12.
24. Silcox, J.; Hirsch, P. B. *Philos. Mag.* **1959**, *4*, 72–89.
25. Matsukawa, Y.; Zinkle, S. J. *Science* **2007**, *318*, 959–962.
26. Osetsky, Y. N.; Bacon, D. J. *Nucl. Instrum. Methods B* **2001**, *180*, 85–90.
27. Osetsky, Y. N.; Serra, A.; Victoria, M.; Golubov, S. I.; Priego, V. *Philos. Mag. A* **1999**, *79*, 2285–2311.
28. Osetsky, Y. N.; Stoller, R. E.; Matsukawa, Y. *J. Nucl. Mater.* **2004**, *329–333*, 1228–1232.
29. Nordlund, K.; Gao, F. *Appl. Phys. Lett.* **1999**, *74*(18), 2720–2722.
30. Kiritani, M. *Mater. Sci. Forum* **1987**, *15–18*, 1023–1046.
31. Kiritani, M. *Mater. Chem. Phys.* **1997**, *50*, 133–138.
32. Sekimura, N.; Kanzaki, Y.; Okada, S. R.; Masuda, T.; Ishino, S. *J. Nucl. Mater.* **1994**, *212–215*, 160–163.
33. Zinkle, S. J.; Wolfer, W. G.; Kulcinski, G. L.; Seitzman, L. E. *Philos. Mag. A* **1987**, *55*(1), 127–140.
34. Norgett, M. J.; Robinson, M. T.; Torrens, I. M. *Nucl. Eng. Des.* **1975**, *33*, 50–54.
35. Oen, O. S. Cross Sections for Atomic Displacements in Solids by Fast Electrons; ORNL-4897; Oak Ridge National Lab: Oak Ridge, TN, 1973; p 204.
36. Doran, D. G.; Graves, N. J. *Displacement Cross Sections and PKA Spectra: Tables and Applications*; HEDL-TME

76–70, Hanford Engineering Development Laboratory: Richland, WA, 1976.
37. Ziegler, J. F.; Biersak, J. P.; Littmark, U. *The Stopping and Range of Ions in Solids*; Pergamon: New York, 1985.
38. Zinkle, S. J.; Singh, B. N. *J. Nucl. Mater.* **1993**, *199*, 173–191.
39. Averback, R. S.; Diaz de la Rubia, T. *Solid State Phys.* **1998**, *51*, 281–402.
40. Schilling, W.; Ullmaier, H. In *Nuclear Materials, Part 2*, Frost, B. R. T., Ed. VCH: Weinheim, Germany, 1992; Vol. 10B, pp 179–241.
41. Yasunaga, K.; Yasuda, K.; Matsumura, S.; Sonoda, T. *Nucl. Instrum. Methods Phys. Res. B* **2008**, *266*(12–13), 2877–2881.
42. Averback, R. S. *J. Nucl. Mater.* **1994**, *216*, 49–62.
43. Diaz de la Rubia, T.; Soneda, N.; Caturla, M. J.; Alonso, E. A. *J. Nucl. Mater.* **1997**, *251*, 13–33.
44. Phythian, W. J.; Stoller, R. E.; Foreman, A. J. E.; Calder, A. F.; Bacon, D. J. *J. Nucl. Mater.* **1995**, *223*, 245–261.
45. Stoller, R. E. *J. Nucl. Mater.* **2000**, *276*, 22–32.
46. Diaz de la Rubia, T.; Phythian, W. J. *J. Nucl. Mater.* **1992**, *191–194*, 108–115.
47. Kiritani, M. *J. Nucl. Mater.* **2000**, *276*(1–3), 41–49.
48. Muroga, T.; Kitajima, K.; Ishino, S. *J. Nucl. Mater.* **1985**, *133–134*, 378–382.
49. Barashev, A. V.; Golubov, S. I. *Philos. Mag.* **2009**, *89*(31), 2833–2860.
50. Golubov, S. I.; Singh, B. N.; Trinkaus, H. *J. Nucl. Mater.* **2000**, *276*, 78–89.
51. Trinkaus, H.; Heinisch, H. L.; Barashev, A. V.; Golubov, S. I.; Singh, B. N. *Phys. Rev. B* **2002**, *66*(6), 060105.
52. Trinkaus, H.; Singh, B. N.; Golubov, S. I. *J. Nucl. Mater.* **2000**, *283–287*, 89–98.
53. Zinkle, S. J.; Sindelar, R. L. *J. Nucl. Mater.* **1988**, *155–157*, 1196–1200.
54. Kiritani, M. *Ultramicroscopy* **1991**, *39*(1–4), 180–186.
55. Kiritani, M.; Takata, H. *J. Nucl. Mater.* **1978**, *69–70*, 277–309.
56. Kiritani, M. *J. Nucl. Mater.* **1994**, *216*, 220–264.
57. Heinisch, H. L.; Singh, B. N. *Philos. Mag. A* **1993**, *67*(2), 407–424.
58. Stoller, R. E., Oak Ridge National Lab, private communication, 2010.
59. Stoller, R. E.; Greenwood, L. R. *J. Nucl. Mater.* **1999**, *271–272*, 57–62.
60. Zinkle, S. J.; Victoria, M.; Abe, K. *J. Nucl. Mater.* **2002**, *307–311*, 31–42.
61. Corbett, J. W. *Electron Radiation Damage in Semiconductors and Metals*. Academic Press: New York, 1966; p 410.
62. Dienes, G. J.; Vineyard, G. H. *Radiation Effects in Solids*; Interscience Publishers: New York, 1957.
63. Schilling, W.; Ehrhart, P.; Sonnenberg, K. In *Fundamental Aspects of Radiation Damage in Metals, CONF-751006-P1*; Robinson, M. T., Young, F. W., Jr., Eds. National Tech. Inform. Service: Springfield, VA, 1975; Vol. I, pp 470–492.
64. Seeger, A. K. In *Radiation Damage in Solids;* IAEA: Vienna, 1962; Vol. 1, pp 101–127.
65. Agullo-Lopez, F.; Catlow, C. R. A.; Townsend, P. D. *Point Defects in Materials*. Academic Press: San Diego, CA, 1988; p 445.
66. Hautojarvi, P.; Pollanen, L.; Vehanen, A.; Yli-Kauppila, J. *J. Nucl. Mater.* **1983**, *114*(2–3), 250–259.
67. Lefevre, J.; Costantini, J. M.; Esnouf, S.; Petite, G. *J. Appl. Phys.* **2009**, *106*(8), 083509.
68. Schultz, H. *Mater. Sci. Eng. A* **1991**, *141*, 149–167.
69. Xu, Q.; Yoshiie, T.; Mori, H. *J. Nucl. Mater.* **2002**, *307–311*(2), 886–890.
70. Mansur, L. K. *J. Nucl. Mater.* **1993**, *206*, 306–323.
71. Sizmann, R. *J. Nucl. Mater.* **1978**, *69–70*, 386–412.
72. Walker, R. M. In *Radiation Damage in Solids*; Billington, D. S., Ed. Academic Press: New York, 1962; pp 594–629.
73. Makin, M. J.; Minter, M. J. *Acta Metall.* **1960**, *8*, 691–699.
74. Shimomura, Y. *J. Nucl. Mater.* **1990**, *174*(2–3), 210–219.
75. Zee, R. H.; Wilkes, P. *Philos. Mag. A* **1980**, *42*(4), 463–482.
76. Jiang, W.; Weber, W. J.; Lian, J.; Kalkhoran, N. M. *J. Appl. Phys.* **2009**, *105*(1), 013529.
77. Schmitz, G.; Ewert, J. C.; Harbsmeier, F.; Uhrmacher, M. *Phys. Rev. B* **2001**, *63*(22), 224113.
78. Birtcher, R. C.; Averback, R. S.; Blewitt, T. H. *J. Nucl. Mater.* **1978**, *75*(1), 167–176.
79. Horak, J. A.; Blewitt, T. H. *J. Nucl. Mater.* **1973**, *49*, 161–180.
80. Horak, J. A.; Blewitt, T. H. *Nucl. Technol.* **1975**, *27*(3), 416–438.
81. Nakagawa, M.; Böning, K.; Rosner, P.; Vogl, G. *Phys. Rev. B* **1977**, *16*(12), 5285–5302.
82. Nakagawa, M.; Mansel, W.; Boning, K.; Rosner, P.; Vogl, G. *Phys. Rev. B* **1979**, *19*(2), 742–748.
83. Birtcher, R. C.; Blewitt, T. H. *J. Nucl. Mater.* **1981**, *98*, 63–70.
84. Birtcher, R. C.; Blewitt, T. H. *J. Nucl. Mater.* **1988**, *152*(2–3), 204–211.
85. Weber, W. J. *J. Am. Ceram. Soc.* **1993**, *76*(7), 1729–1738.
86. Hobbs, L. W.; Sreeram, A. N.; Jesurum, C. E.; Berger, B. A. *Nucl. Instrum. Methods B* **1996**, *116*, 18–25.
87. Lam, N.; Okamoto, P. R.; Li, M. *J. Nucl. Mater.* **1997**, *251*, 89–97.
88. Sabochick, M. J.; Lam, N. *Phys. Rev. B* **1991**, *43*(7), 5243–5252.
89. Wendler, E.; Bilani, O.; Gärtner, K.; *et al. Nucl. Instrum. Methods Phys. Res. B* **2009**, *267*(16), 2708–2711.
90. Yoshida, N.; Kiritani, M. *J. Phys. Soc. Jpn.* **1973**, *35*(5), 1418–1429.
91. Zinkle, S. J.; Snead, L. L.; Eatherly, W. S.; Jones, J. W.; Hensley, D. K. In *Microstructural Processes During Irradiation*; Zinkle, S. J., Lucas, G. E., Ewing, R. C., Williams, J. S., Eds. Materials Research Society: Warrendale, PA, 1999; Vol. 540, pp 305–310.
92. Singh, B. N.; Evans, J. H. *J. Nucl. Mater.* **1995**, *226*, 277–285.
93. Singh, B. N.; Zinkle, S. J. *J. Nucl. Mater.* **1993**, *206*, 212–229.
94. Zinkle, S. J. *Radiat. Eff. Defects Solids* **1999**, *148*, 447–477.
95. Hashimoto, N.; Byun, T. S.; Farrell, K.; Zinkle, S. J. *J. Nucl. Mater.* **2004**, *329–333*, 947–952.
96. Hashimoto, N.; Byun, T. S.; Farrell, K. *J. Nucl. Mater.* **2006**, *351*(1–3), 295–302.
97. Diaz de la Rubia, T.; Averback, R. S.; Hsieh, H.; Benedek, R. *J. Mater. Res.* **1989**, *4*(3), 579–586.
98. Flynn, C. P.; Averback, R. S. *Phys. Rev. B* **1988**, *38*(10), 7118–7120.
99. Eldrup, M.; Singh, B. N.; Zinkle, S. J.; Byun, T. S.; Farrell, K. *J. Nucl. Mater.* **2002**, *307–311*, 912–917.
100. Zinkle, S. J.; Singh, B. N. *J. Nucl. Mater.* **2006**, *351*, 269–284.
101. Li, M.; Eldrup, M.; Byun, T. S.; Hashimoto, N.; Snead, L. L.; Zinkle, S. J. *J. Nucl. Mater.* **2008**, *376*(1), 11–28.
102. Eldrup, M.; Li, M.; Snead, L. L.; Zinkle, S. J. *Nucl. Instrum. Methods Phys. Res. B* **2008**, *266*(16), 3602–3606.
103. Rowcliffe, A. F.; Lee, E. H. *J. Nucl. Mater.* **1982**, *108–109*, 306–318.

104. Kai, J. J.; Klueh, R. L. *J. Nucl. Mater.* **1996**, *230*, 116–123.
105. Klueh, R. L.; Harries, D. R. *High-Chromium Ferritic and Martensitic Steels for Nuclear Applications*. American Society for Testing and Materials: West Conshohocken, PA, 2001; p 221.
106. Maziasz, P. J. *J. Nucl. Mater.* **1989**, *169*, 95–115.
107. Zinkle, S. J.; Farrell, K.; Kanazawa, H. *J. Nucl. Mater.* **1991**, *179–181*, 994–997.
108. Garner, F. A.; Hamilton, M. L.; Shikama, T.; Edwards, D. J.; Newkirk, J. W. *J. Nucl. Mater.* **1992**, *191–194*, 386–390.
109. Garner, F. A.; Toloczko, M. B.; Sencer, B. H. *J. Nucl. Mater.* **2000**, *276*, 123–142.
110. Zinkle, S. J.; Farrell, K. *J. Nucl. Mater.* **1989**, *168*, 262–267.
111. Maksimkin, O. P.; Tsai, K. V.; Turubarova, L. G.; Doronina, T.; Garner, F. A. *J. Nucl. Mater.* **2004**, *329–333*, 625–629.
112. Maksimkin, O. P.; Tsai, K. V.; Turubarova, L. G.; Doronina, T.; Garner, F. A. *J. Nucl. Mater.* **2007**, *367–370*, 990–994.
113. Porollo, S. I.; Konobeev, Y. V.; Dvoriashin, A. M.; Vorobjev, A. N.; Krigan, V. M.; Garner, F. A. *J. Nucl. Mater.* **2002**, *307–311*, 339–342.
114. Adda, Y. In *Radiation-Induced Voids in Metals*; Corbett, J. W., Ianniello, L. C., Eds. National Technical Information Service: Springfield, VA, 1972; pp 31–81.
115. Budylkin, N.; Mironova, E. G.; Chernov, V. M.; Krasnoselov, V. A.; Porollo, S. I.; Garner, F. A. *J. Nucl. Mater.* **2008**, *375*(3), 359–364.
116. Garner, F. A.; Greenwood, L. R.; Edwards, D. J. *J. Nucl. Mater.* **1994**, *212–215*, 426–430.
117. Garner, F. A.; Stubbins, J. F. *J. Nucl. Mater.* **1994**, *212–215*, 1298–1302.
118. Singh, B. N.; Trinkaus, H. *J. Nucl. Mater.* **1992**, *186*, 153–165.
119. Trinkaus, H.; Singh, B. N. *J. Nucl. Mater.* **2003**, *323*(2–3), 229–242.
120. Ullmaier, H. *Nucl. Fusion* **1984**, *24*(8), 1039–1083.
121. Klabunde, C. E.; Coltman, R. R., Jr. *J. Nucl. Mater.* **1982**, *108–109*, 183–193.
122. Jenkins, M. L.; Kirk, M. A.; Phythian, W. J. *J. Nucl. Mater.* **1993**, *205*, 16–30.
123. Phythian, W. J.; English, C. A.; Yellen, D. H.; Bacon, D. J. *Philos. Mag. A* **1991**, *63*(5), 821–833.
124. Zinkle, S. J. In *15th Int. Symp. on Effects of Radiation on Materials, ASTM STP 1125*, Stoller, R. E., Kumar, A. S., Gelles, D. S., Eds. American Society for Testing and Materials: Philadelphia, PA, 1992; pp 749–763.
125. Bacon, D. J. *J. Nucl. Mater.* **1993**, *206*(2–3), 249–265.
126. Griffiths, M. *J. Nucl. Mater.* **1993**, *205*, 225–241.
127. Roof, R. B., Jr.; Ranken, W. A. *J. Nucl. Mater.* **1975**, *55*, 357–358.
128. Woo, C. H. *J. Nucl. Mater.* **2000**, *276*, 90–103.
129. Keilholtz, G. W.; Moore, R. E. *Nucl. Applic.* **1967**, *3*, 686–691.
130. Fukumoto, K.; Kimura, A.; Matsui, H. *J. Nucl. Mater.* **1996**, *258–263*, 1431–1436.
131. Garner, F. A.; Gelles, D. S.; Takahashi, H.; Ohnuki, S.; Kinoshita, H.; Loomis, B. A. *J. Nucl. Mater.* **1992**, *191–194*, 948–951.
132. Snead, L. L.; Burchell, T. D.; Katoh, Y. *J. Nucl. Mater.* **2008**, *381*(1–2), 55–61.
133. Gelles, D. S. *J. Nucl. Mater.* **1996**, *233–237*, 293–298.
134. Lee, E. H.; Mansur, L. K. *Metall. Trans. A* **1990**, *21*(5), 1021–1035.
135. Kim, I.-S.; Hunn, J. D.; Hashimoto, N.; *et al. J. Nucl. Mater.* **2000**, *280*(3), 264–274.
136. Naguib, H. M.; Kelly, R. *Radiat. Effects* **1975**, *25*, 1–12.
137. Trachenko, K. *J. Phys.: Condens. Matter* **2004**, *16*(49), R1491–R1515.
138. Inui, H.; Mori, H.; Fujita, H. *Acta Metall.* **1989**, *37*(5), 1337–1342.
139. Zinkle, S. J.; Snead, L. L. *Nucl. Instrum. Methods B* **1996**, *116*, 92–101.
140. Sickafus, K. E.; Grimes, R. W.; Valdez, J. A.; *et al. Nature Mater.* **2007**, *6*(3), 217–223.
141. Sickafus, K. E.; Minervini, L.; Grimes, R. W.; *et al. Science* **2000**, *289*(5480), 748–751.
142. Schroeder, K. *Radiat. Effects* **1970**, *5*, 255–263.
143. Thompson, L. J.; Youngblood, G.; Sosin, A. *Radiat. Effects* **1973**, *20*, 111–134.
144. Wollenberger, H. J. In *Vacancies and Interstitials in Metals*; Seeger, A., Schumacher, D., Schilling, W., Diehl, J., Eds. North-Holland: Amsterdam, 1970; pp 215–254.
145. Kiritani, M. *J. Nucl. Mater.* **1989**, *169*, 89–94.
146. Zinkle, S. J. *J. Nucl. Mater.* **1987**, *150*, 140–158.
147. Motta, A. T.; Olander, D. R. *Acta Metall. Mater.* **1990**, *38*(11), 2175–2185.
148. Snead, L. L.; Zinkle, S. J.; Eatherly, W. S.; Hensley, D. K.; Vaughn, N. L.; Jones, J. W. In *Microstructural Processes During Irradiation*; Zinkle, S. J., Lucas, G. E., Ewing, R. C., Williams, J. S., Eds. Materials Research Society: Warrendale, PA, 1999; Vol. 540, pp 165–170.
149. Mansur, L. K. *Nucl. Technol.* **1978**, *40*(1), 5–34.
150. Mansur, L. K. *J. Nucl. Mater.* **1994**, *216*, 97–123.
151. Mansur, L. K.; Coghlan, W. A. *J. Nucl. Mater.* **1983**, *119*(1), 1–25.
152. Trinkaus, H. *J. Nucl. Mater.* **1983**, *118*(1), 39–49.
153. Trinkaus, H. *J. Nucl. Mater.* **1985**, *133–134*, 105–112.
154. Garner, F. A. *J. Nucl. Mater.* **1983**, *117*, 177–197.
155. Glowinski, L. D.; Fiche, C.; Lott, M. *J. Nucl. Mater.* **1973**, *47*(3), 295–310.
156. Lanore, J. M.; Glowinski, L.; Risbet, A.; *et al.* In *Fundamental Aspects of Radiation Damage in Metals, CONF-751006-P2*; Robinson, M. T., Young, F. W., Jr., Eds. National Tech. Inform. Service: Springfield, VA, 1975; Vol. II, pp 1169–1180.
157. Singh, B. N.; Zinkle, S. J. *J. Nucl. Mater.* **1994**, *217*(1–2), 161–171.
158. Smidt, F. A., Jr.; Reed, J. R.; Sprague, J. A. In *Radiation Effects in Breeder Reactor Structural Materials*; Bleiberg, M. L., Bennett, J. W., Eds. TMS-AIME: New York, 1977; pp 337–346.
159. Zinkle, S. J.; Skuratov, V. A.; Hoelzer, D. T. *Nucl. Instrum. Methods B* **2002**, *191*, 758–766.
160. Egerton, R. F.; Li, P.; Malac, M. *Micron* **2004**, *35*(6), 399–409.
161. Itoh, N.; Stoneham, A. M. *Materials Modification by Electronic Excitation*. Cambridge University Press: Cambridge, UK, 2001; pp 1–536.
162. Itoh, N.; Tanimura, K.; Nakai, Y. *Nucl. Instrum. Methods B* **1992**, *65*, 21–25.
163. Sibley, W. A. *Nucl. Instrum. Methods B* **1984**, *1*(2–3), 419–426.
164. Bourgoin, J. C. *Radiat. Eff. Defects Solids* **1989**, *111–112*(1–2), 29–36.
165. Bourgoin, J. C.; Corbett, J. W. *J. Chem. Phys.* **1973**, *59*(8), 4042–4046.
166. Bourgoin, J. C.; Corbett, J. W. *Radiat. Effects* **1978**, *36*, 157–188.
167. Corbett, J. W.; Bourgoin, J. C. *IEEE Trans. Nucl. Sci.* **1971**, *18*(6), 11–20.
168. Kimerling, L. C. *Solid-State Electron* **1978**, *21*, 1391–1401.
169. Zinkle, S. J. *J. Nucl. Mater.* **1995**, *219*, 113–127.
170. Zinkle, S. J. In *Microstructure Evolution During Irradiation*; Robertson, I. M., Was, G. S., Hobbs, L. W.,

Diaz de la Rubia, T., Eds. Materials Research Society: Pittsburgh, PA, 1997; Vol. 439, pp 667–678.
171. Dammak, H.; Dunlop, A.; Lesueur, D. *Nucl. Instrum. Methods Phys. Res. B* **1996**, *107*(1–4), 204–211.
172. Szenes, G. *Phys. Rev. B* **1995**, *51*(13), 8026–8029.
173. Toulemonde, M.; Dufour, C.; Meftah, A.; Paumier, E. *Nucl. Instrum. Methods B* **2000**, *166–167*, 903–912.
174. Toulemonde, M.; Trautmann, C.; Balanzat, E.; Hjort, K.; Weidinger, A. *Nucl. Instrum. Methods Phys. Res. B* **2004**, *216*, 1–8.
175. Wang, Z. G.; Dufour, C.; Paumier, E.; Toulemonde, M. *J. Phys.: Condens. Matter* **1994**, *6*(34), 6733–6750.
176. Zinkle, S. J.; Skuratov, V. A. *Nucl. Instrum. Methods B* **1998**, *141*(1–4), 737–746.
177. Ramos, S. M. M.; Bonardi, N.; Canut, B.; Della-Negra, S. *Phys. Rev. B* **1998**, *57*(1), 189–193.
178. Szenes, G. *J. Nucl. Mater.* **2005**, *336*(1), 81–89.
179. Toulemonde, M.; Bouffard, S.; Studer, F. *Nucl. Instrum. Methods B* **1994**, *91*(1–4), 108–123.
180. Wesch, W.; Kamarou, A.; Wendler, E. *Nucl. Instrum. Meth. B* **2004**, *225*(1–2), 111–128.
181. Pellerin, N.; Dodane-Thiriet, C.; Montouillout, V.; Beauvy, M.; Massiot, D. *J. Phys. Chem. B* **2007**, *111*(44), 12707–12714.
182. Zinkle, S. J.; Matzke, H.; Skuratov, V. A. In *Microstructural Processes During Irradiation*; Zinkle, S. J., Lucas, G. E., Ewing, R. C., Williams, J. S., Eds. Materials Research Society: Warrendale, PA, 1999; Vol. 540, pp 299–304.
183. Audouard, A.; Mamy, R.; Toulemonde, M.; Szenes, G.; Thome, L. *Nucl. Instrum. Methods Phys. Res. B* **1998**, *146*(1–4), 217–221.
184. Skuratov, V. A.; Zinkle, S. J.; Efimov, A. E.; Havancsak, K. *Surf. Coat. Technol.* **2005**, *196*(1–3), 56–62.
185. Dunlop, A.; Lesueur, D.; Legrand, P.; Dammak, H. *Nucl. Instrum. Methods Phys. Res. B* **1994**, *90*(1–4), 330–338.
186. Iwase, A.; Ishino, S. *J. Nucl. Mater.* **2000**, *276*, 178–185.
187. Itoh, N.; Duffy, D. M.; Khakshouri, S.; Stoneham, A. M. *J. Phys.: Condens. Matter* **2009**, *21*(47), 474205.
188. Matzke, H.; Lucuta, P. G.; Wiss, T. *Nucl. Instrum. Methods B* **2000**, *166–167*, 920–926.
189. Sickafus, K. E.; Matzke, H.; Yasuda, K.; *et al. Nucl. Instrum. Methods B* **1998**, *141*, 358–365.
190. Szenes, G.; Horvath, Z. E.; Pecz, B.; Paszti, F.; Toth, L. *Phys. Rev. B* **2002**, *65*(4), 045206.
191. Matzke, H. *Nucl. Instrum. Methods B* **1996**, *116*, 121–125.
192. Toulemonde, M.; Costantini, J. M.; Dufour, C.; Meftah, A.; Paumier, E.; Studer, F. *Nucl. Instrum. Methods B* **1996**, *116*(1–4), 37–42.
193. Johnson, R. A.; Lam, N. Q. *Phys. Rev. B* **1976**, *13*(10), 4364–4375.
194. Johnson, R. A.; Lam, N. Q. *J. Nucl. Mater.* **1978**, *69–70*, 424–433.
195. Marwick, A. D. *J. Phys. F: Metal Phys.* **1978**, *8*(9), 1849–1861.
196. Okamoto, P. R.; Rehn, L. E. *J. Nucl. Mater.* **1979**, *83*(1), 2–23.
197. Okamoto, P. R.; Wiedersich, H. *J. Nucl. Mater.* **1974**, *53*(1), 336–345.
198. Wiedersich, H.; Okamoto, P. R.; Lam, N. Q. *J. Nucl. Mater.* **1979**, *83*(1), 98–108.
199. Lee, E. H.; Maziasz, P. J.; Rowcliffe, A. F. In *Phase Stability during Irradiation*; Holland, J. R., Mansur, L. K., Potter, D. I., Eds. The Metallurgical Society of AIME: New York, 1981; pp 191–218.
200. Maziasz, P. J. *J. Nucl. Mater.* **1993**, *205*, 118–145.
201. Badger, B., Jr.; Plumton, D. L.; Zinkle, S. J.; *et al.* In *12th Int. Symp. on Effects of Radiation on Materials, ASTM STP 870*; Garner, F. A., Perrin, J. S., Eds. American Society for Testing and Materials: Philadelphia, PA, 1985; Vol. I, pp 297–316.
202. Plumton, D. L.; Wolfer, W. G. *J. Nucl. Mater.* **1984**, *120*(2–3), 245–253.
203. Whitley, J. B. Depth Dependent Damage in Heavy Ion Irradiated Nickel. University of Wisconsin, Madison, 1978.
204. Brager, H. R.; Garner, F. A. *J. Nucl. Mater.* **1978**, *73*(1), 9–19.
205. Lee, E. H.; Rowcliffe, A. F.; Kenik, E. A. *J. Nucl. Mater.* **1979**, *83*(1), 79–89.
206. Williams, T. M.; Titchmarsh, J. M.; Arkell, D. R. *J. Nucl. Mater.* **1982**, *107*(2–3), 222–244.
207. Porter, D. L. *J. Nucl. Mater.* **1979**, *79*(2), 406–411.
208. Mansur, L. K.; Lee, E. H. *J. Nucl. Mater.* **1991**, *179–181*, 105–110.
209. Snead, L. L.; Zinkle, S. J.; Hay, J. C.; Osborne, M. C. *Nucl. Instrum. Methods B* **1998**, *141*, 123–132.
210. Jackson, K. A. *J. Mater. Res.* **1988**, *3*(6), 1218–1226.
211. Jagielski, J.; Thome, L. *Vacuum* **2007**, *81*(10), 1352–1356.
212. Trinkaus, H. *Mater. Sci. Forum* **1997**, *248–249*, 3–12.
213. Weber, W. J. *Nucl. Instrum. Methods Phys. Res. B* **2000**, *166*, 98–106.
214. Koike, J.; Mitchell, T. E.; Parkin, D. M. *Appl. Phys. Lett.* **1991**, *59*(20), 2515–2517.
215. Bement, A. L., Jr. In *Radiation Effects (Metallurgical Society Conf.)*; Sheely, W. F., Ed. Gordon and Breach: New York, 1967; Vol. 37, pp 671–725.
216. Byun, T. S.; Farrell, K. *Acta Mater.* **2004**, *52*, 1597–1608.
217. Diehl, J.; Seidel, G. P. In *Radiation Damage in Reactor Materials;* IAEA: Vienna, 1969; Vol. I, pp 187–214.
218. Little, E. A. *Int. Met. Rev.* **1976**, *21*, 25–60.
219. Lucas, G. E. *J. Nucl. Mater.* **1993**, *206*, 287–305.
220. Maki, M. J. In *Radiation Effects (Metallurgical Society Conf.)*; Sheely, W. F., Ed. Gordon and Breach: New York, 1967; Vol. 37, pp 627–669.
221. Wechsler, M. S. In *Fundamental Aspects of Radiation Damage in Metals, CONF-751006-P2*; Robinson, M. T., Young, F. W., Jr., Eds. National Tech. Inform. Service: Springfield, VA, 1975; Vol. II, pp 991–1009.
222. Zinkle, S. J.; Lucas, G. E. In *Fusion Materials Semiann.* Progress Report for Period ending June 30, 2003, DOE/ER-0313/34; Oak Ridge National Lab, 2003; pp 101–125.
223. Majumdar, S.; Kalinin, G. *J. Nucl. Mater.* **2000**, *283–287*, 1424–1428.
224. Rice, P. M.; Zinkle, S. J. *J. Nucl. Mater.* **1998**, *258–263*, 1414–1419.
225. Rowcliffe, A. F.; Zinkle, S. J.; Stubbins, J. F.; Edwards, D. J.; Alexander, D. J. *J. Nucl. Mater.* **1998**, *258–263*, 183–192.
226. Izumi, K.; Yasuda, K.; Kinoshita, C.; Katsuwada, M. *J. Nucl. Mater.* **1998**, *258–263*, 1817–1821.
227. Zinkle, S. J. *J. Am. Ceram. Soc.* **1989**, *72*(8), 1343–1351.
228. Katoh, Y.; Snead, L. L.; Nozawa, T.; Kondo, T.; Busby, J. T. *J. Nucl. Mater.* **2010**, *403*(1–3), 48–61.
229. Dienst, W. *J. Nucl. Mater.* **1992**, *191–194*, 555–559.
230. Dienst, W.; Zimmermann, H. *J. Nucl. Mater.* **1994**, *212–215*, 1091–1095.
231. Hollenberg, G. W.; Henager, C. H., Jr.; Youngblood, G. E.; *et al. J. Nucl. Mater.* **1995**, *219*, 70–86.
232. Oliver, W. C.; McHargue, C. J.; Zinkle, S. J. *Thin Solid Films* **1987**, *153*, 185–196.
233. Fabritsiev, S. A.; Pokrovsky, A. S.; Zinkle, S. J.; *et al. J. Nucl. Mater.* **1996**, *233–237*, 526–533.
234. Frost, H. M.; Kennedy, J. C. *J. Nucl. Mater.* **1986**, *141–143*, 169–173.

235. Zinkle, S. J.; Fabritsiev, S. A. *Atomic Plasma Mater. Interact. Data Fusion (supplement to Nucl. Fusion)* **1994**, *5*, 163–192.
236. Edwards, D. J.; Garner, F. A.; Greenwood, L. R. *J. Nucl. Mater.* **1994**, *212–215*, 404–409.
237. Snead, L. L.; Zinkle, S. J.; White, D. P. *J. Nucl. Mater.* **2005**, *340*, 187–202.
238. Hillel, A. J.; Rossiter, P. L. *Philos. Mag. B* **1981**, *44*(3), 383–388.
239. Klaffky, R. W.; Rose, B. H.; Goland, A. N.; Dienes, G. J. *Phys. Rev. B* **1980**, *21*(8), 3610–3634.
240. Pells, G. P. *J. Nucl. Mater.* **1991**, *184*(3), 183–190.
241. Rose, A. *Concepts in Photoconductivity and Allied Problems*. Interscience: New York, 1963; p 168.
242. van Lint, V. A. J.; Flanagan, T. M.; Leadon, R. E.; Nabor, J. A.; Rogers, V. C. *Mechanisms of Radiation Effects in Electronic Materials;* Wiley: New York, 1980; Vol. 1, p 359.
243. Zinkle, S. J.; Hodgson, E. R. *J. Nucl. Mater.* **1992**, *191–194*, 58–66.
244. Klemens, P. G.; Hurley, G. F.; Clinard, F. W., Jr. In *Proc. 2nd Topical Meeting on the Technology of Controlled Nuclear Fusion, CONF-760935*; Kulcinski, G. L., Burleigh, N. M., Eds. National Tech. Inform. Service: Springfield, VA, 1976; pp 957–964.
245. Morelli, D. T.; Perry, T. A.; Farmer, J. W. *Phys. Rev. B* **1993**, *47*(1), 131–139.
246. White, D. P. *J. Appl. Phys.* **1993**, *73*(5), 2254–2258.
247. Odette, G. R.; Nanstad, R. K. *J. Met.* **2009**, *61*(7), 17–23.
248. Phythian, W. J.; English, C. A. *J. Nucl. Mater.* **1993**, *205*, 162–177.
249. Boothby, R. M. *J. Nucl. Mater.* **1996**, *230*(2), 148–157.
250. Dubuisson, P.; Gilbon, D.; Seran, J. L. *J. Nucl. Mater.* **1993**, *205*, 178–189.
251. Nemoto, Y.; Hasegawa, A.; Satou, M.; Abe, K.; Hiraoka, Y. *J. Nucl. Mater.* **2004**, *324*(1), 62–70.
252. Odette, G. R.; Lucas, G. E. *Radiat. Eff. Defects Solids* **1998**, *144*, 189–231.
253. Bruemmer, S. M.; Simonen, E. P.; Scott, P. M.; Andresen, P. L.; Was, G. S.; Nelson, J. L. *J. Nucl. Mater.* **1999**, *274*(3), 299–314.
254. Bruemmer, S. M.; Was, G. S. *J. Nucl. Mater.* **1994**, *216*, 348–363.
255. Scott, P. *J. Nucl. Mater.* **1994**, *211*(2), 101–122.
256. Was, G. S.; Busby, J. T. *Philos. Mag.* **2005**, *85*(4–7), 443–465.
257. Johnson, R. A.; Lam, N. Q. *Phys. Rev. B* **1977**, *15*(4), 1794–1800.
258. Lam, N. Q.; Okamoto, P. R.; Wiedersich, H. *J. Nucl. Mater.* **1978**, *74*(1), 101–113.
259. Holt, R. A. *J. Nucl. Mater.* **1980**, *90*(1–3), 193–204.
260. Garner, F. A.; Toloczko, M. B.; Greenwood, L. R.; Eiholzer, C. R.; Paxton, M. M.; Puigh, R. J. *J. Nucl. Mater.* **2000**, *283–287*, 380–385.
261. Hickman, B. S.; Walker, D. S. *Proc. Br. Ceram. Soc.* **1967**, *7*, 381–389.
262. Hickman, B. S. In *Studies in Radiation Effects, Series A: Physical and Chemical*; Dienes, G. J., Ed. Gordon and Breach: New York, 1966; Vol. 1, pp 72–158.
263. Snead, L. L.; Zinkle, S. J. In *Space Technology and Applications International Forum-STAIF 2005 (AIP Conf. Proc.)*; El-Genk, M. S., Ed. American Institute of Physics: Melville, NY, 2005; Vol. 746, pp 768–775.
264. Matthews, J. R.; Finnis, M. W. *J. Nucl. Mater.* **1988**, *159*, 257–285.
265. Grossbeck, M. L.; Ehrlich, K.; Wassilew, C. *J. Nucl. Mater.* **1990**, *174*, 264–281.
266. Jung, P. *J. Nucl. Mater.* **1993**, *200*(1), 138–140.
267. Jung, P. *J. Nucl. Mater.* **1983**, *113*(2–3), 133–141.
268. Stoller, R. E.; Grossbeck, M. L.; Mansur, L. K. In *15th Int. Symp. on Effects of Radiation on Materials*; Stoller, R. E., Kumar, A. S., Gelles, D. S., Eds. American Society for Testing and Materials: Philadelphia, PA, 1992; pp 517–529.
269. Mattas, R. F.; Garner, F. A.; Grossbeck, M. L.; Maziasz, P. J.; Odette, G. R.; Stoller, R. E. *J. Nucl. Mater.* **1984**, *122–123*, 230–235.
270. Garner, F. A. In *Nuclear Materials*; Frost, B. R. T., Ed. VCH: New York, 1994; Vol. 10A, pp 419–543.
271. Fish, R. L.; Straalsund, J. L.; Hunter, C. W.; Holmes, J. J. In *Effects of Radiation on Substructure and Mechanical Properties of Metals and Alloys*; Moteff, J., Ed. American Society for Testing and Materials: Philadelphia, PA, 1973; pp 149–164.
272. Clinard, F. W., Jr.; Hurley, G. F.; Hobbs, L. W. *J. Nucl. Mater.* **1982**, *108–109*, 655–670.
273. Yamada, R.; Zinkle, S. J.; Pells, G. P. *J. Nucl. Mater.* **1994**, *209*, 191–203.
274. Schroeder, H.; Stamm, U. In *Effects of Radiation on Materials: 14th International Symposium, ASTM STP 1046*; Packan, N. H., Stoller, R. E., Kumar, A. S., Eds. American Society for Testing & Materials: Philadelphia, PA, 1990; Vol. 1046, pp 223–245.
275. Ullmaier, H. *J. Nucl. Mater.* **1985**, *133–134*, 100–104.
276. Schroeder, H.; Batfalsky, P. *J. Nucl. Mater.* **1983**, *117*, 287–294.
277. Mansur, L. K.; Grossbeck, M. L. *J. Nucl. Mater.* **1988**, *155–157*, 130–147.
278. van der Schaaf, B.; de Vries, M. I.; Elen, J. D. In *Radiation Effects in Breeder Reactor Structural Materials*; Bleiberg, M. L., Bennett, J. W., Eds. TMS-AIME: New York, 1977; pp 307–316.
279. Braski, D. N.; Schroeder, H.; Ullmaier, H. *J. Nucl. Mater.* **1979**, *83*, 265–277.
280. Bloom, E. E.; Wiffen, F. W. *J. Nucl. Mater.* **1975**, *58*(2), 171–184.
281. Kramer, D.; Brager, H. R.; Rhodes, C. G.; Pard, A. G. *J. Nucl. Mater.* **1968**, *25*(2), 121–131.
282. Kesternich, W. *J. Nucl. Mater.* **1985**, *127*(2–3), 153–160.
283. Schroeder, H. *J. Nucl. Mater.* **1988**, *155–157*, 1032–1037.
284. Yamamoto, N.; Nagakawa, J.; Murase, Y.; Shiraishi, H. *J. Nucl. Mater.* **1998**, *258–263*, 1634–1638.
285. Kimura, A.; Kasada, R.; Morishita, K.; *et al. J. Nucl. Mater.* **2002**, *307–311*, 521–526.
286. Schroeder, H.; Ullmaier, H. *J. Nucl. Mater.* **1991**, *179–181*, 118–124.
287. Yamamoto, N.; Murase, Y.; Nagakawa, J. *Fusion Eng. Des.* **2006**, *81*(8–14), 1085–1090.
288. Shiraishi, H.; Yamamoto, N.; Hasegawa, A. *J. Nucl. Mater.* **1989**, *169*, 198–205.
289. Atteridge, D. G.; Charlot, L. A.; Johnson, A. B., Jr.; Remark, J. F. In *Radiation Effects and Tritium Technology for Fusion Reactors, CONF-750989*; Watson, J. S., Wiffen, F. W., Eds. USERDA: Gatlinburg, TN, 1976; pp 307–330.
290. Sagues, A. A.; Auer, J. In *Radiation Effects and Tritium Technology for Fusion Reactors, CONF-750989*; Watson, J. S., Wiffen, F. W., Eds. USERDA: Gatlinburg, TN, 1976; pp 331–343.
291. Wiffen, F. W. In *Radiation Effects and Tritium Technology for Fusion Reactors, CONF-750989*; Watson, J. S., Wiffen, F. W., Eds. USERDA: Gatlinburg, TN, 1976; Vol. II, pp 344–361.
292. Carpenter, G. J. C.; Nicholson, R. B. In *Radiation Damage in Reactor Materials;* IAEA: Vienna, 1969; Vol. II, pp 383–400.

293. Fabritsiev, S. A.; Pokrovsky, A. S.; Zinkle, S. J.; Edwards, D. J. In *19th Int. Symp. on Effects of Radiation on Materials*; Hamilton, M. L., Kumar, A. S., Rosinski, S. T., Grossbeck, M. L., Eds. American Society for Testing and Materials: West Conshohocken, PA, 2000; pp 1226–1242.
294. Kirk, M. A.; Robertson, I. M.; Jenkins, M. L.; English, C. A.; Black, T. J.; Vetrano, J. S. *J. Nucl. Mater.* **1987**, *149*, 21–28.
295. Gelles, D. S.; Garner, F. A.; Brager, H. R. In *10th Int. Symp. on Effects of Radiation on Materials*; Kramer, D., Brager, H. R., Perrin, J. S., Eds. American Society for Testing and Materials: Philadelphia, PA, 1981; pp 735–753.
296. Zinkle, S. J. *J. Nucl. Mater.* **1992**, *191–194*, 645–649.
297. Ghoniem, N. M.; Walgraef, D.; Zinkle, S. J. *J. Comp.-Aided Mater. Des.* **2001**, *8*(1), 1–38.
298. Jäger, W.; Trinkaus, H. *J. Nucl. Mater.* **1993**, *205*, 394–410.
299. Seeger, A.; Jin, N. Y.; Phillipp, F.; Zaiser, M. *Ultramicroscopy* **1991**, *39*, 342–354.
300. Katoh, Y.; Hashimoto, N.; Kondo, S.; Snead, L. L.; Kohyama, A. *J. Nucl. Mater.* **2006**, *351*, 228–240.
301. Zinkle, S. J.; Pells, G. P. *J. Nucl. Mater.* **1998**, *253*, 120–132.
302. Zinkle, S. J.; Horsewell, A.; Singh, B. N.; Sommer, W. F. *J. Nucl. Mater.* **1994**, *212–215*, 132–138.
303. Zinkle, S. J.; Singh, B. N. *J. Nucl. Mater.* **2000**, *283–287*, 306–312.
304. Zinkle, S. J.; Snead, L. L. *J. Nucl. Mater.* **1995**, *225*, 123–131.
305. Satoh, Y.; Yoshiie, T.; Mori, H.; Kiritani, M. *Phys. Rev. B* **2004,** *69*, 0941081–11.
306. Jenkins, M. L.; Zhou, Z.; Dudarev, S. L.; Sutton, A. P.; Kirk, M. A. *J. Mater. Sci.* **2006**, *41*(14), 4445–4453.
307. Kojima, S.; Satoh, Y.; Taoka, H.; Ishida, I.; Yoshiie, T.; Kiritani, M. *Philos. Mag. A* **1989**, *59*(3), 519–532.
308. Yao, Z.; Schäublin, R.; Victoria, M. *J. Nucl. Mater.* **2003**, *323*(2–3), 388–393.
309. Yoshida, N.; Muroga, T.; Watanabe, H.; Araki, K.; Miyamoto, Y. *J. Nucl. Mater.* **1988**, *155–157*, 1222–1226.
310. Dai, Y. Mechanical properties and microstructures of copper, gold and palladium single crystals irradiated with 600 MeV protons. Lausanne, EPFL, 1995.
311. Horsewell, A.; Singh, B. N.; Proennecke, S.; Sommer, W. F.; Heinisch, H. L. *J. Nucl. Mater.* **1991**, *179–181*, 924–927.
312. Victoria, M.; Baluc, N.; Bailat, C.; *et al. J. Nucl. Mater.* **2000**, *276*, 114–122.
313. Horiki, M.; Arai, S.; Satoh, Y.; Kiritani, M. *J. Nucl. Mater.* **1998**, *255*(2–3), 165–173.
314. Okada, A.; Kanao, K.; Yoshiie, T.; Kojima, S. *Mater. Trans. JIM* **1989**, *30*(4), 265–272.
315. Byun, T. S.; Hashimoto, N.; Farrell, K. *J. Nucl. Mater.* **2006**, *351*(1–3), 303–315.
316. Farrell, K.; Byun, T. S.; Hashimoto, N. *J. Nucl. Mater.* **2004**, *335*(3), 471–486.
317. Wechsler, M. S. In *The Inhomogeneity of Plastic Deformation*; Reed-Hill, R. E., Ed. American Society for Metals: Metals Park, OH, 1972; pp 19–54.
318. Byun, T. S.; Farrell, K.; Hashimoto, N. *J. Nucl. Mater.* **2004**, *329–333*, 998–1002.
319. Hashimoto, N.; Ando, M.; Tanigawa, H.; Sawai, T.; Shiba, K.; Klueh, R. L. *Fusion Sci. Technol.* **2003**, *44*(2), 490–494.
320. Hashimoto, N.; Zinkle, S. J.; Rowcliffe, A. F.; Robertson, J. P.; Jitsukawa, S. *J. Nucl. Mater.* **2000**, *283–287*, 528–534.
321. Luft, A. *Prog. Mater. Sci.* **1991**, *35*, 97–204.
322. Byun, T. S.; Farrell, K.; Li, M. *Acta Mater* **2008**, *56*(5), 1044–1055.
323. Byun, T. S.; Farrell, K.; Li, M. *Acta Mater* **2008**, *56*(5), 1056–1064.
324. Byun, T. S.; Hashimoto, N.; Farrell, K. *Acta Mater.* **2004**, *52*, 3889–3899.
325. Sharp, J. V. *Radiat. Effects* **1972**, *14*, 71–75.
326. Byun, T. S.; Hashimoto, N.; Farrell, K.; Lee, E. H. *J. Nucl. Mater.* **2006**, *349*, 251–264.
327. Matsukawa, Y.; Osetsky, Y. N.; Stoller, R. E.; Zinkle, S. J. *Philos. Mag.* **2008**, *88*(4), 581–597.
328. Osetsky, Y. N.; Rodney, D.; Bacon, D. J. *Philos. Mag.* **2006**, *86*(16), 2295–2313.
329. Lee, H.-J.; Wirth, B. D. *Philos. Mag.* **2009**, *89*(9), 821–841.
330. Nogaret, T.; Rodney, D.; Fivel, M.; Robertson, C. *J. Nucl. Mater.* **2008**, *380*(1–3), 22–29.
331. Rodney, D. *Nucl. Instrum. Methods Phys. Res. B* **2005**, *228*, 100–110.
332. Foreman, A. J. E.; Sharp, J. V. *Philos. Mag.* **1969**, *19*, 931.
333. Lee, E. H.; Byun, T. S.; Hunn, J. D.; Yoo, M. H.; Farrell, K.; Mansur, L. K. *Acta Mater.* **2001**, *49*, 3277–3287.
334. Jaouen, C.; Delafond, J.; Riviere, J. P. *J. Phys. F: Metal Phys.* **1987**, *17*(2), 335–350.
335. Jencic, I.; Bench, M. W.; Robertson, I. M.; Kirk, M. A. *J. Appl. Phys.* **1995**, *78*(2), 974–982.
336. Wang, S. X.; Wang, L. M.; Ewing, R. C. *Phys. Rev. B* **2001**, *63*(2), 024105.
337. Wang, L. M.; Wang, S. X.; Ewing, R. C.; *et al. Mater. Sci. Eng. A* **2000**, *286*, 72–80.
338. English, C. A.; Jenkins, M. L. *J. Nucl. Mater.* **1981**, *96*(3), 341–357.
339. Jiang, W.; Bae, I. T.; Weber, W. J. *J. Phys.: Condens. Matter* **2007**, *19*(35), 356207.
340. Kondo, S.; Katoh, Y.; Snead, L. L. *Appl. Phys. Lett.* **2008**, *93*(16), 163110.
341. Mruzik, M. R.; Russell, K. C. *Surf. Sci.* **1977**, *67*, 205–225.
342. Gelles, D. S.; Claudson, R. M.; Thomas, L. E. Quantitative Analysis of Void Swelling. Fusion Reactor Materials Semiannual Progress Report for Period ending September 30, 1987, DOE/ER-0313/3, Oak Ridge National Lab, 1987; pp 131–136.
343. Mansur, L. K.; Lee, E. H.; Maziasz, P. J.; Rowcliffe, A. F. *J. Nucl. Mater.* **1986**, *141–143*, 633–646.
344. Evans, J. H. *Nature* **1971**, *229*(5284), 403–404.
345. Evans, J. H. In *Patterns, Defects and Materials Instabilities*; Walgraef, D., Ghoniem, N. M., Eds. Kluwer Academic: Amsterdam, 1990; pp 347–370.
346. Risbet, A.; Levy, V. *J. Nucl. Mater.* **1974**, *50*(1), 116–118.
347. Zinkle, S. J.; Kojima, S. *J. Nucl. Mater.* **1991**, *179–181*, 395–398.
348. Chen, L. J.; Ardell, A. J. *J. Nucl. Mater.* **1978**, *75*, 177–185.
349. Farrell, K.; Packan, N. H. *J. Nucl. Mater.* **1979**, *85–86*, 683–687.
350. Horsewell, A.; Singh, B. N. *Radiat. Effects* **1987**, *102*, 1–5.
351. Mazey, D. J.; Francis, S.; Hudson, J. A. *J. Nucl. Mater.* **1973**, *47*, 137–142.
352. Semenov, A. A.; Woo, C. H.; Frank, W. *Appl. Phys. A* **2008**, *93*(2), 365–377.
353. Loomis, B. A.; Gerber, S. B.; Taylor, A. *J. Nucl. Mater.* **1977**, *68*, 19–31.